Master Thesis

Quark spectral functions at finite temperature in a Dyson-Schwinger approach

B.Sc. Christian Andreas Welzbacher

September 2012

Institute for Theoretical Physics
Justus-Liebig-Universität Giessen

Nature uses only the longest threads to weave her patterns, so that each small piece of her fabric reveals the organization of the entire tapestry.

(Richard P. Feynman)

Contents

1 Introduction

One important tool towards understanding the thermodynamic processes of any kind of matter is the corresponding phase diagram. The phase diagram is an instrument to visualize, depending on the temperature and the pressure, which states or phases the particular matter can occupy; it helps not only to understand the different characteristics of each phase but also the transitions in between.
One may think the phase diagram of water is the most important one since water it is the basis of all life. Yet there is another phase diagram which is even more fundamental: the phase diagram of Quantum chromodynamics (QCD), a theory that describes the strong force. This force is responsible for the existence of protons and neutrons which eventually form, together with electrons, all matter. The current understanding of the QCD phase diagram, shown Fig.1.1, implies not only the phase of ordinary matter but, among others, also the so called Quark Gluon Plasma (QGP). This is a state of matter one could have observed a short time after the big bang at very high temperatures and low density. The QGP reveals much interesting information about how our universe has formed, whether QCD is a valid description of the strong interaction and about certain symmetries which are very important to understand underlying principles. An extended overview is given in the textbook of Letessier and Rafelski [1].

In order to investigate the QGP experimentally one has to set up large accelerators (i.e. the LHC in Geneva/Switzerland, RHIC in Brookhaven/USA or the future SIS300 as part of FAIR at GSI in Darmstadt/Germany) and observe the collision of heavy ions (such as lead or gold). During the experiment the ions are accelerated to such high energies that the zone of the collision becomes very hot and dense hence reproducing the conditions characteristic to QGP. Later on the QGP will cool down due to spatial expansion and converts to regular strong interacting matter with the usual degrees of freedom, the so called hadrons. Within the QGP phase the degrees of freedom are free quarks and gluons which one cannot observe in the hadronic phase due to the fundamental principle of confinement.
In this work we mainly investigate the quark spectral function, which is a relevant quantity helping to understand the QGP close to and above the transition temperature. In this strongly coupled regime just above the phase transition quarks are still suggested to be quasiparticle excitations. The spectral function encodes information about the relevant degrees of freedom, some of their attributes and the interaction in the system. Additionally, one can derive certain predictions for experimental observables to compare the results to the available data and it can be used as input

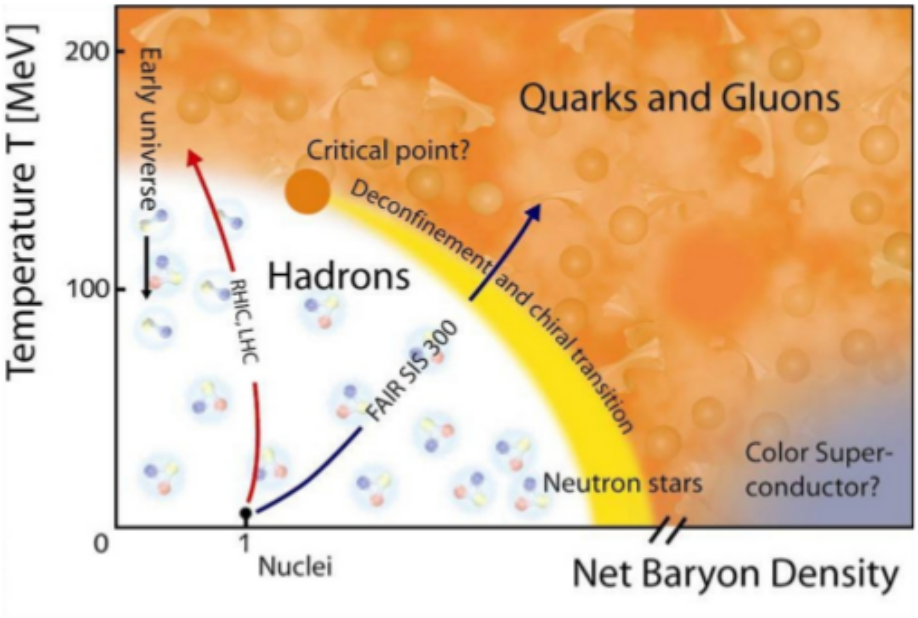

Figure 1.1: Schematic picture of the QCD phase diagram taken from [2].

for transport approaches as discussed in [3, 4]. One can calculate the spectral function from the quark two-point function. This function, also called quark propagator, contains information about how a quark moves and reacts throughout a medium.
Since in the year 2000, when the CERN laboratory announced that there is conclusive evidence for a new state of matter, the interest in the QGP on experimental as well as on theoretical side has rapidly increased. High quality data from RHIC as well as from the LHC became available and the investigation of the QCD phase diagram became more and more intensive (see [5,6] and [7] for review). However, perturbation theory (which exploits the so called asymptotic freedom, indicating weak coupling at small distances, to express necessary quantities in orders of the interaction strength), fails near the phase transition for QGP since the (running) coupling constant is of order one, leading to an expansion where every term is of the same order.
A first approach to QCD at finite temperature has been proposed by Braaten and Pisarski and is based on a resummed perturbation theory [8–10]. The so called hard thermal loop (HTL) method is designed for the case of weak coupling and high temperatures, and used to calculate (effective) quantities in hot gauge theories. It can also be used to predict a HTL effective quark propagator, the quark spectral function and experimental observables related to the production of soft dileptons [11]. In this context a high temperature prediction for the quark spectral function has been found, revealing two branches of quasiparticle excitations. One of them is connected to the quark, while the other is a collective excitation which partly shows antiparticle

like behavior and was dubbed plasmino, referring to a similar phenomenon in QED plasma called plasmon.
Since the HTL method is designed for high temperature, far above the expected transition temperatures, other techniques must be employed. One possible approach to do calculations of thermodynamical quantities for the QGP is the AdS/CFT correspondence. A summary of the current status can be found in [12]. There are qualitative results, for example for the shear viscosity of the medium or Quarkonium states, but its not yet possible to make exact quantitative predictions.
Lattice QCD and the usage of modern supercomputers represents an alternative approach to investigate properties of QCD at finite temperature, in particular the quark propagator and the corresponding spectral function (for more details refer e.g. to the textbook [13]). In lattice QCD correlation functions are calculated on a four dimensional grid with three spatial and one time (inverse temperature) direction. The lattice quark propagator in Landau gauge at finite temperature was first investigated by Hamada et al. [14]. Consecutive studies of the propagator as well as the spectral properties have been studied by Karsch, Kacymarek et al. [15, 16] and recently in [17]. The authors used an ansatz motivated by the HTL results for the spectral function and fitted this to the propagator calculated on the lattice. Unfortunately, calculations on the lattice can only be done for a simplified case of QCD where the Yang-Mills part (gluons) does not depend on the fermionic part (but vice versa). This case where no quark loops are taken into account is called quenched QCD, while the scheme including this backcoupling is called unquenched QCD. Moreover, exact calculations are only possible for zero chemical potential due to the sign problem in the exponential of the effective action. There is no solution to this problem yet and only predictions from model calculations are available [18, 19]. Other approaches use effective models such as the Nambu-Jona-Lasinio (*NJL*) model [20].
In this thesis we use the non-perturbative functional approach of Dyson-Schwinger equations (*DSE*s) which have been used successfully to investigate fundamental questions like confinement in Yang-Mills theory but also to more phenomenological research on hadron observables [21–24]. For our studies, of particular interest are the applications to finite temperature and chemical potential (see for example [25] for a review). There are some using model ansätze for the quark-gluon vertex in the so called rainbow-ladder approximation, which takes into account only bare vertices [26, 27]. This is also done in [28] where a technique called Maximum-Entropy-Method (*MEM*) is applied to derive the quark spectral function from the quark propagator, which in turn is calculated from the QCD gap equation in rainbow approximation. Recent considerations and calculations for quenched and two-flavor QCD phase transitions can be found in [29–31]. Most recently an investigation for the unquenched case with two plus one quark flavors for finite temperature and chemical potential has been performed in [32]. Finally, in [33] spectral functions are investigated in a Dyson-Schwinger framework by employing the technique used in investigations on the lattice, namely to fit certain ansätze of the spectral function

to the obtained quark propagator. This will serve as a foundation for investigations of the spectral function in the quenched and, along with [32], for the $N_F = 2 + 1$ unquenched case. In all investigations we limit ourself to zero chemical potential, e.g. the temperature axis of Fig.1.1, where one expects a phase transition from ordinary hadronic matter to the QGP phase.
The thesis is organized as follows: In the next chapter we review some general aspects of QCD, in particular a thermodynamic formulation and the QCD phase diagram. We then also focus on the Dyson-Schwinger equations as the equations of motion of the quark propagator in Matsubara formalism and our truncation, which is motivated by the analysis of the phase diagram from [32]. A recap of the HTL formalism and the definition of the spectral functions, which themselves depend on the quark correlator, is given. At the end we briefly introduce the Schwinger function used to investigate positivity violations of the spectral function.
chapter 3 is dedicated to the numerical background. We introduce the Levenberg-Marquardt method, which is employed to fit the given ansätze for the quark spectral function to the quark correlator. We give the parameters entering the equations as well as detailed discussions of the models for the quark-gluon vertex, followed by a brief comparison of quenched and unquenched propagators. Finally, we present our ansätze for the spectral function.
In chapter 4 we consider the case of quenched QCD and test our routine by comparing our findings to the results from [33]. Furthermore, we extend the investigations to higher temperatures by employing the introduced vertex parameters. Additionally, we work with an improved ansatz for the spectral function in the chiral limit as well as for finite quark masses.
The case of unquenched QCD is subject of chapter 5. In this thesis, the quark spectral function for unquenched $N_F = 2 + 1$ QCD is calculated in the chiral limit and for physical masses in a Dyson-Schwinger framework. Since this calculation is not possible on the lattice, we investigate different ansätze to explore the spectral properties. For both cases, the behavior of the Schwinger function calculated from our obtained spectral function is studied.
In chapter 6 we summarize our results and indicate possible directions for future work.

2 QCD at finite temperature

In this work, we are interested in properties of strongly interacting matter at high temperatures. Firstly we want to focus on general aspects of QCD and its phase diagram. We discuss some properties and related topics such as symmetries and phase transitions. Next we set the foundation for the detailed understanding of finite temperature QCD in form of a brief review of a formulation at thermodynamic equilibrium. This is followed by a summary of the Dyson-Schwinger framework and truncation scheme we use, based on [32]. A short review of HTL calculations is given before we draw our attention to the quark spectral function, the object of our main interest, and eventually to the Schwinger function.

2.1 The QCD phase diagram and aspects of QCD

An important quantity of a theory, revealing all necessary informations to derive predictions for the included particles or fields, is the Lagrangian or Lagrangian density. For QCD including the non-abelian Yang-Mills sector, this object can be derived from fundamental principles such as Poincaré invariance, locality, certain symmetries and renormalizability. In a very compressed notation the QCD Lagrangian density is written as

$$\mathcal{L}_{QCD}[\Psi, \overline{\Psi}, A] = \overline{\Psi}\left(i\not{D} - m\right)\Psi - \frac{1}{2g_s^2}\mathrm{Tr}_c(F_{\mu\nu}F^{\mu\nu}) \tag{2.1}$$

with the quark fields Ψ and $\overline{\Psi}$, the field strength tensor $F_{\mu\nu} = [D_\mu, D_\nu]$ and the common notation $\not{D} = \gamma^\mu D_\mu$, using the known Dirac γ-matrices and the covariant derivative $D_\mu = \partial_\mu + A_\mu$. The coupling constant is absorbed into the gluon field A_μ in a standard way. One needs to read this equation carefully due to the suppression of most of the indices. The mass matrix m for example, represents the diagonal matrix m=diag(m_u, m_d, m_s,...) with the current quark masses generated by electroweak interactions. The spinors of the quark field transform under a gauge transformation as elements of the fundamental representation of SU(3) while the gauge fields may be written as $A_\mu = -it^a A_\mu^a$ with the generators of the group t^a.
One important symmetry which is interesting for considerations of the phase diagram of QCD is the chiral symmetry. Chirality is an attribute of a particle, which determines whether the particle transforms under a left or right handed representation of

the Poincaré group. Since Dirac spinors are a superposition of both representations, one considers the projections onto the left, respectively right handed Weyl spinors

$$\Psi_{R,L} = \frac{1}{2}(1 \pm \gamma_5)\Psi \tag{2.2}$$

as chirality eigenstates and rewrites the quark part of the Lagrangian in Eq.(2.1) as

$$\overline{\Psi}\left(i\not{D} - m\right)\Psi = \overline{\Psi}_L\left(-i\not{D}\right)\Psi_L + \overline{\Psi}_R\left(-i\not{D}\right)\Psi_R + \overline{\Psi}_L m\Psi_R + \overline{\Psi}_R m\Psi_L, \tag{2.3}$$

where m once again is the diagonal matrix, including entries according to the number N_f of quark flavors under consideration. For m=0, which is referred to as the chiral limit, it is apparent from Eq.(2.3) that the right and left handed quarks decouple and the Lagrangian is invariant under global $U_L(N_f) \times U_R(N_f)$ transformations.
For convenience, one reorganizes this by defining axial- and vector-transformations leading to the underlying symmetry group of $SU_A(N_f) \times SU_V(N_f) \times U_A(1) \times U_V(1)$ (see [2]). We now want to consider three different ways chiral symmetry can be broken:

- **Explicit chiral symmetry breaking:** The quark masses generated by the electroweak interaction break the chiral symmetry explicitly, which follows immediately from Eq.(2.3).
- **Spontaneous chrial symmetry breaking:** Even for m=0 the gluon interactions generate quark masses dynamically, a purely non-perturbative phenomenon.
- **Breaking of axial $U_A(1)$ symmetry:** Quantizing the theory leads to an implicit breaking of the axial $U_A(1)$ symmetry, even in the chiral limit. This is also referred to as the $U_A(1)$ anomaly.

While the explicit breaking of chiral symmetry is independent of the respective phase, the breaking of chiral symmetry with respect to dynamical mass generation is restored for certain chiral phase transitions. Since spontaneous chiral symmetry breaking and the $U_A(1)$ anomaly are dominant even away from the chiral limit, one expects to see effects in certain order parameters such as the one for chiral symmetry, the chiral condensate. Taking also the transitions between confined and deconfined phases into account, which are reflected in the (dressed) Polyakov loop as an order parameter, one can distinguish different phases in the QCD phase diagram.
For zero chemical potential the so-called Columbia plot shows the mass and flavor dependence of the chiral and deconfinement phase transitions. This plot is shown in Fig.2.1, where the gray area and the blue line in the left part of the diagram deal with the chiral phase transition, while the upper right part shows the deconfinement phase transition.

A detailed explanation of the plot can be found in [34] as well as in [2]. Here we want to focus on the three cases we are concerned with in this work:

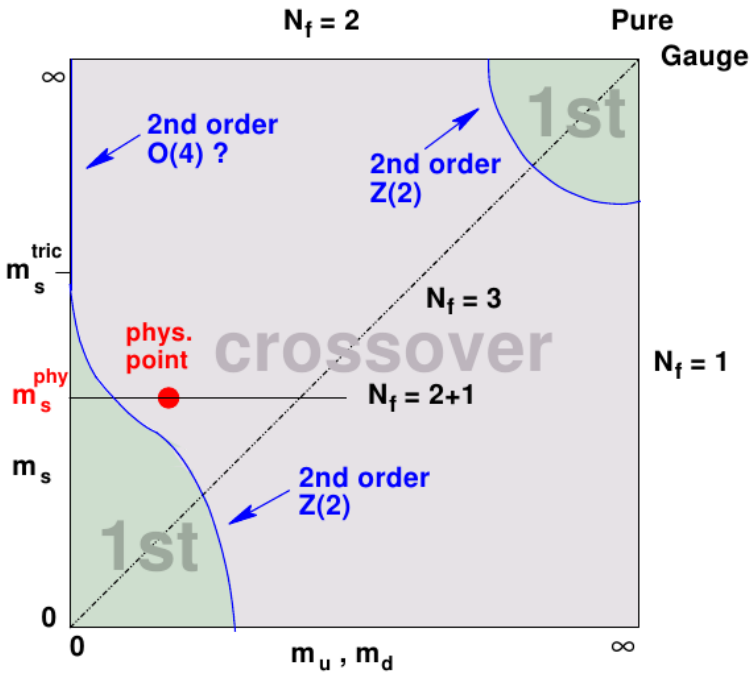

Figure 2.1: Expected phase diagram at zero quark chemical potential taken from [34].

1. **Quenched QCD:** This scenario may be found in the upper right corner of Fig.2.1, since infinite heavy quarks do not effect the Yang-Mills sector. From the plot we expect a first order phase transition implying a discontinuity in the order parameter.

2. **Unquenched QCD in the chiral limit:** To find the type of transition for this case, where the up and down quark bare masses are zero, the exact position of the tri-critical strange quark mass with respect to the physical one is important, but still unresolved. The question is whether we see a first or a second order phase transition. In our case we will face a second order phase transition, where the first derivative of the order parameter is discontinuous.

3. **Unquenched QCD for physical masses:** The physical point is clearly indicated in Fig.2.1 and we see that a crossover rather than a sharp transition is expected.

Finally we want to come back to the QCD phase diagram in Fig.1.1, where the case shown in the Columbia plot refers to the $\mu = 0$ axis. QCD is in the chirally broken and confined phase for low temperatures and densities where the well known hadronic bound states and resonances are located. At large enough temperatures and chemical potential QCD undergoes a chiral and a deconfining phase transition

towards QGP. Other phases present in this scheme, e.g. the regime where the interior of neutron stars is expect to be described (high densities and low temperatures) and a possible quark-matter superconducting phase, are also shown. One key question concerning the phase diagram of QCD is the exact position of the critical end point for the chiral transition. The sketch also shows the patterns, by which RHIC and the future SIS300 at FAIR explore the phase diagram experimentally.

2.2 Imaginary time formalism

If we want to investigate QCD at finite temperature we need to develop a formalism, which makes quantities of interest depending on the temperature in equilibrium accessible. A lot of textbooks and previous works are concerned with this topic. We follow the main steps of [35] to introduce the idea of one way to set up such a formalism on the example of scalar fields, before we give the result for QCD.
In statistical mechanics one learns there are three ensembles to describe different types of systems. The microcanonical ensemble is used for isolated systems with fixed energy, particle number and volume while the canonical ensemble describes a system in contact with a heat bath. For our purpose, the most interesting one is the grand canonical ensemble which also takes particle exchange into account. In this case the statistical density matrix is defined as

$$\hat{\rho} = e^{-\beta\left(\hat{H}-\sum_i \mu_i N_i\right)} \tag{2.4}$$

with the inverse temperature $\beta = \frac{1}{k_B T}$, the conserved quantities N_i and the according chemical potentials μ_i, introduced as the Lagrange multipliers. For convenience, we work in units with the Boltzmann factor k_B set to one. For the field operator $\phi(\mathbf{x}, t)$, we denote a complete set of orthonormal eigenstates as $|\phi\rangle$. The partition function, as a central quantity, is defined as

$$\mathcal{Z} = \mathrm{Tr}\hat{\rho} = \sum_a \int d\phi_a \ \langle\phi_a|e^{-\beta\left(\hat{H}-\mu N\right)}|\phi_a\rangle, \tag{2.5}$$

where the sum runs over all states. To make a connection to a functional integral representation, we consider the transition amplitude for a particular state $|\phi'\rangle$ going into the same state after some time t_f, and introduce an evolution in imaginary time $t = -i\tau$. The transition amplitude is expressed in terms of the time evolution operator $e^{-i\hat{H}t_f}$ as

$$\langle\phi'|e^{-i\hat{H}t_f}|\phi'\rangle. \tag{2.6}$$

Next, the interval [0,t_f] is divided in N subintervals. Alternating between the field and the conjugate field momentum operator, using their completeness and the orthonormality, a complete set of eigenstates is inserted at each time interval. Since

the size Δt of each interval becomes very small for $N \to \infty$ the exponential $e^{-i\hat{H}\Delta t}$ can be expanded. One arrives at

$$\langle \phi' | e^{-i\hat{H}t_f} | \phi' \rangle = N \cdot \int_{\phi(\mathbf{x},0)=\phi'(\mathbf{x})}^{\phi(\mathbf{x},t_f)=\phi'(\mathbf{x})} [\mathrm{d}\phi] \; exp\left(i \int_0^{t_f} dt \int d^3x \; \mathcal{L}(t) \right) \tag{2.7}$$

where the factor of N comes from the unrestricted integration over the conjugate momentum, $[\mathrm{d}\phi]$ represents a functional integral and we already introduced the Lagrangian density (a detailed derivation can be found in [35]).
If we compare Eqs.(2.5) and (2.7), we notice that the partition function can be expressed in terms of functional integrals if we make the analytic continuation $t_f \to -i\beta$. By additionally performing the analytical continuation for the variable $t \to -i\tau$ with $0 \leq \tau \leq \beta$ we eventually arrive at the main result

$$\mathcal{Z} = \int_{periodic} [d\phi] \; exp\left(- \int_0^{\beta} d\tau \int d^3x \; \mathcal{L}_E(\tau, \mathbf{x}) \right), \tag{2.8}$$

where the Euclidean Lagrangian density is defined as $\mathcal{L}_E(\tau, \mathbf{x}) = -\mathcal{L}(t = -i\tau, \mathbf{x})$ and the subscript "periodic" indicates the implementation of periodic boundary conditions in τ direction, since we work with a scalar field (compare Eq.(2.7)):

$$\phi(\tau = 0) = \phi(\tau = \beta).$$

The same procedure can be used to develop a representation of fermions. This differs only in the character of the boundary conditions, which are antiperiodic due to the anticommuting character of the fermion fields. The boundary conditions in the fermionic case read

$$\Psi(\tau = 0) = -\Psi(\tau = \beta).$$

For the QCD partition function we find

$$\mathcal{Z}[J_\mu, \overline{\eta}, \eta] = \int [d\Psi] \; [d\overline{\Psi}][dA] exp\left(-\mathcal{S}_E[\Psi, \overline{\Psi}, A_\mu] + \int_0^{\beta} d\tau \int d^3x \; \left(A_\mu^a J_\mu^a + \overline{\eta}\Psi + \overline{\Psi}\eta \right) \right) \tag{2.9}$$

with the Euclidean action

$$\begin{aligned} \mathcal{S}_E[\Psi, \overline{\Psi}, A_\mu] &= \int_0^{\beta} d\tau \int d^3x \; \mathcal{L}_E \qquad (2.10) \\ &= \int_0^{\beta} d\tau \int d^3x \left(\overline{\Psi} \left(-i\not{D} + m \right) \Psi + \frac{1}{2g_s^2} \mathrm{Tr}_c(F_{\mu\nu} F^{\mu\nu}) \right). \end{aligned}$$

The gluons, as bosons, obey periodic boundary conditions and the quarks antiperiodic ones. Among the introduced source terms in Eq.(2.9) are Grassmann variables $\eta, \overline{\eta}$ for the fermions and a source J_μ^a for the gauge fields. Finally, we introduce the

Matsubara formalism, connected to the Fourier transform of a function in imaginary time. Due to the periodic character we expect a discrete corresponding variable. For a function f, periodic in the imaginary-time direction, $f(\tau) = f(\tau + \beta)$, we define the Fourier transformation by

$$\begin{aligned} f(\tau) &= T \sum_{n=-\infty}^{\infty} e^{-i\widetilde{\omega}_n \tau} f(i\widetilde{\omega}_n) \\ f(i\widetilde{\omega}_n) &= \int_0^\beta d\tau \; e^{i\widetilde{\omega}_n \tau} f(\tau) \end{aligned} \tag{2.11}$$

where

$$\widetilde{\omega}_n = 2n \; \pi \; T \tag{2.12}$$

is the bosonic Matsubara frequency. In the case of a fermionic function obeying antiperiodic boundary conditions $\Psi(\tau) = -\Psi(\tau + \beta)$, the Matsubara frequency is of the form

$$\omega_n = (2n + 1) \; \pi \; T. \tag{2.13}$$

For this work we follow the conventions from Ref. [33] for the Dirac γ-matrices

$$\begin{aligned} \gamma_4 &= -\gamma_0^M \\ \gamma_j &= -i\gamma_j^M. \end{aligned} \tag{2.14}$$

We define the four-vector shorthand notation $k = (\omega_n, \mathbf{k})$, which differs from the Euclidean definition in a minus sign in the fourth component. In calculations involving this vector we have

$$\int \frac{d^4k}{(2\pi)^4} f(ik_4, \mathbf{k}) \to T \sum_n \int \frac{d^3k}{(2\pi^3} f(i\omega_n, \mathbf{k}). \tag{2.15}$$

where we already used explicitly imaginary arguments in the functions, as we will do throughout the whole work, reminding of the conventions in (2.14).

2.3 QCD Dyson-Schwinger equations

Within this work, we aim at a description of the quark spectral function in the QGP using the functional approach of Dyson-Schwinger equations, where n-point functions, such as for the quark, the gluon and the quark-gluon vertex, can be calculated by self-consistently solving an infinite tower of coupled integral equations. Since it is impossible to solve the whole (infinite) set of equations in general, one has to make certain approximations. This process, called truncation, needs to be done carefully

in order to describe the relevant physics correctly. Guidance for the approximations can be obtained from symmetries, conservation laws and comparison with lattice results. By working with DSEs we obtain a description of dynamical chiral symmetry breaking and the direct accessibility of the Yang-Mills sector, opposing to effective models.
The truncation scheme and setup we use are the same as those used by Lücker and Fischer [32], in our case at zero chemical quark potential. Since their results are also of main interest and importance for our investigations, in the following we introduce the used Dyson-Schwinger framework by a summary of their work in [32].
Their investigations aim for the QCD phase diagram for $N_f = 2$ and $N_f = 2 + 1$ quark flavors at finite temperature and chemical potential, where the notation 2 + 1 indicates two light quarks and a strange quark flavor with vanishing chemical potential for the strange quark.

The in-medium propagators in Landau gauge at finite temperature and chemical potential for the quark and the gluon are given by

$$S(p) = [i(\omega_n + i\mu)\gamma_4 C(p) + i\mathbf{p}\boldsymbol{\gamma} A(p) + B(p)]^{-1} \tag{2.16}$$

$$D_{\mu\nu}(p) = P^L_{\mu\nu}(p)\frac{Z^L(p)}{p^2} + P^T_{\mu\nu}(p)\frac{Z^T(p)}{p^2}. \tag{2.17}$$

In this case the vector dressing functions A and C, as well as the scalar dressing function B of the quark propagator, depend on the momentum $p = (\omega_n, \mathbf{p})$, and so are the gluon dressing functions Z_L and Z_T. "L" and "T" indicate longitudinal respectively transversal orientation with respect to the heat bath, obtained with the projectors given by

$$P^T_{\mu\nu} = (1 - \delta_{\mu 4})(1 - \delta_{\nu 4})\left(\delta_{\mu\nu} - \frac{p_\mu p_\nu}{\mathbf{p}^2}\right), \tag{2.18}$$

$$P^L_{\mu\nu} = P_{\mu\nu} - P^T_{\mu\nu}.. \tag{2.19}$$

The Matsubara frequencies, defined in Eqs.(2.12) and (2.13), differ for the fermionic (quark) and bosonic (gluon) case. The quantity μ in Eq.(2.16) denotes the quark chemical potential which will be set to zero throughout our work.
We briefly mentioned order parameters as important quantities to describe phase transitions. An order parameter and its first derivative with respect to the temperature are used to define the class of a phase transition. For chiral symmetry breaking the so-called quark (chiral) condensate is a strict order parameter in the chiral limit and indicates a chiral phase transition for finite bare quark masses. The condensate in the DSE framework is defined as

$$\langle\overline{\Psi}\Psi\rangle = Z_2^W T \sum_n \int \frac{d^3p}{(2\pi)^3} \mathrm{Tr}_D[S(p)], \tag{2.20}$$

where Z_2^W is the wave function renormalization constant. As mentioned in [32] this object is quadratically divergent for finite quark masses and can be regularized by defining

$$\Delta_{u,d,s} = \langle\overline{\Psi}\Psi\rangle_{u,d} - \frac{m_{u,d}}{m_s}\langle\overline{\Psi}\Psi\rangle_s, \tag{2.21}$$

dubbed the regularized condensate.

The quark and the gluon DSE

In figure 2.2 we find a diagrammatic representation of the quark DSE, which depends on the (fully) dressed gluon propagator as well as on the full quark-gluon vertex. Those two quantities have to be approximated in our scheme. If we look at Fig.2.3 we see the untruncated full gluon DSE. As pointed out in [32] and Refs. therein, solving this equation turns out to be very difficult. Therefore a truncation is applied involving the quenched gluon propagator calculated on the lattice in [24], represented diagrammatically in Fig.2.4, where the term "quenched" implies that all quark loops are neglected (the last diagram in Fig.2.3). The unquenching, e.g. the inclusion of the quark loop is done by merely adding it to the quenched lattice part. This process neglects all contributions from the quark loop to ghost loops or gluon loops and is in this sense an approximation. In [32] they tested the agreement for vacuum predictions and found agreement on a five percent level. However, in our setup we will observe effects of the quenched part even in unquenched calculations. Since the gluon propagators on the lattice are calculated only for certain temperatures, a fit in T of the dressing functions obtained from the lattice results is necessary and we will come back to this point in the next chapter.
For the truncated scenario of $N_F = 2+1$ unquenched QCD, the quark and the gluon DSE read

$$\left[S^f(p)\right]^{-1} = Z_W^f \left[S_0^f(p)\right]^{-1} + C_F Z_W^f Z_{1F}^f g_s^2 \int\!\!\!\!\!\!\sum_l \gamma_\mu S^f(l)\Gamma_\nu^f(l^2,p^2,q^2)D_{\mu\nu}(q),$$

$$D_{\mu\nu}^{-1}(p) = \left[D_{\mu\nu}^{que.}(p)\right]^{-1} - \sum_f^{N_f} \frac{Z_W^f}{2} g_s^2 \int\!\!\!\!\!\!\sum_l \mathrm{Tr}\left[\gamma_\mu S^f(l)\Gamma_\nu(l^2,q^2,p^2)S^f(q)\right],$$

with $S^f(p)$ being the quark propagator for one of the flavors $f = u,d,s$, $C_F = \frac{4}{3}$ the Casimir operator and Γ_ν the dressed quark-gluon vertex. Additionally, we have the vertex and wave-function renormalization constant Z_{1F} and Z_W and the renormalized coupling $g_s^2 = 4\pi\alpha_s$. The sum over the Matsubara frequencies as well as the integration over the loop three-momentum $\boldsymbol{l}$ is represented by

$$\int\!\!\!\!\!\!\sum_l = T\sum_n \int \frac{d^3l}{(2\pi)^3}.$$

This system of coupled integral equations needs to be solved iteratively to receive the desired dressing functions. In the quenched case, the quark loop in the gluon DSE is not considered, therefore we are left with the quenched lattice data for the gluon propagator.

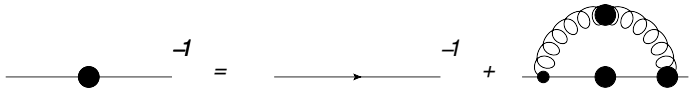

Figure 2.2: Diagrammatic representation of the DSE for the quark propagator where blobs denote dressed propagators respectively vertices (taken from [32])

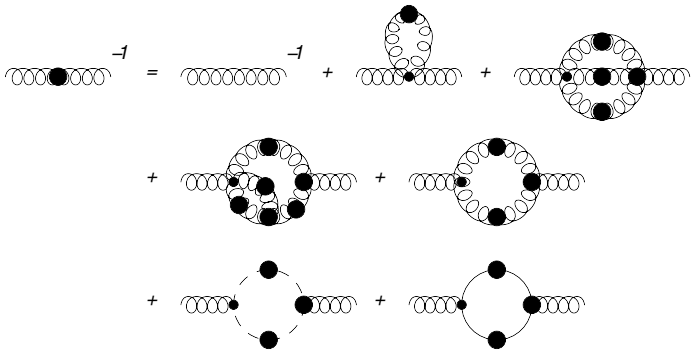

Figure 2.3: Diagrammatic representation of the DSE for the gluon propagator where blobs denote dressed propagators respectively dressed vertices (taken from [32])

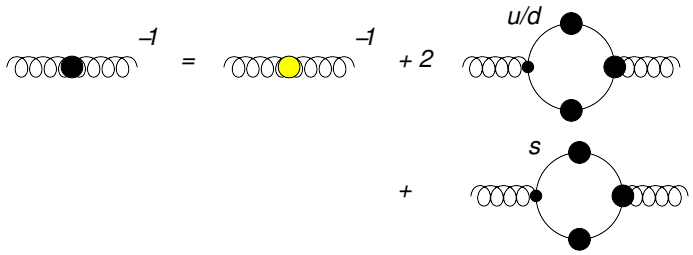

Figure 2.4: Diagrammatic representation of the truncated DSE for the gluon propagator where black blobs denote dressed propagators respectively vertices and the yellow blob the quenched propagator (taken from [32])

Finally, we want to emphasize the implications of the unquenching process. The including of the back-reactions from the quark to the gluonic sector introduces an implicit dependence on the quark chemical potential as well as on the chiral dynamics of the quarks for the gluon dressing functions. This dependences will manifest

predominantly in effects on the thermal mass of the gluon, in particular close to the chiral phase transition.

The quark-gluon vertex

At this point we are left with a definition of the quark gluon vertex, which is part of our truncation scheme. We follow [32] and use an educated guess motivated by basically two constraints:

- The vertex in principle has to satisfy its Slavnov-Taylor identity, which is an not yet resolved issue in QCD. The corresponding Abelian constraint, the Ward-Takahashi identity, has been used to express one part of the vertex in terms of the quark dressing functions, reflected in the first term of the Ball-Chiu vertex.
- In order to have the correct ultraviolet running of the vertex in combination with the gluon dressing functions and to absorb non-Abelian effects the infrared enhanced function $\Gamma(p^2, k^2, q^2)$ is introduced.

Our ansatz for the quark-gluon vertex then reads

$$\begin{aligned} \Gamma_\mu(p,k;q) &= \gamma_\mu \cdot \Gamma(p^2,k^2,q^2) \cdot \left(\delta_{\mu,4} \frac{C(p)+C(q)}{2} + \delta_{\mu,i} \frac{A(p)+A(q)}{2} \right), \\ \Gamma(p^2,k^2,q^2) &= \frac{d_1}{d_2+x} + \frac{x}{\Lambda^2+x} \left(\frac{\beta_0 \alpha(\mu) \ln[x/\Lambda^2+1]}{4\pi} \right)^{2\delta}, \end{aligned} \tag{2.22}$$

where p and k are the fermion momenta and q is the gluon momentum. The three quantities d_1, d_2 and Λ are parameters adjusted to control the renormalization group running of the vertex in the large and low momentum region (d_2 and Λ) and to control the actual strength of the quark gluon interaction at small momenta in the case of d_1. In the ultraviolet, $\delta = (-9N_c)/(44N_c - 8N_f)$ is the anomalous dimension of the vertex and $\beta_0 = (11N_c - 2N_f)/3$, leading to values of $\delta = -9/44$ and $\beta = 11$ in the quenched and $\delta = -1/4$ and $\beta = 9$ in the $N_f = 2+1$ unquenched case. The values of the parameters are fixed as

$$\begin{aligned} \Lambda &= 1.4 \text{ GeV}, \\ d_1^{unq} &= 7.5 \text{ GeV}^2, \\ d_1^{que} &= 4.6 \text{ GeV}^2, \\ d_2 &= 0.5 \text{ GeV}^2. \end{aligned}$$

The variable x, representing a squared momentum, is equal to q^2 in the quark DSE and equal to $p^2 + k^2$ in the quark loop. As it turns out, the parameter d_1 needs to be modified above the crossover respectively critical temperatures for quenched and unquenched calculations. We deal with this issue in the next chapter.

As mentioned before not all unquenching effects for the gluon propagator are taken into account in our truncation scheme. Furthermore there are also effects in the chosen vertex, which can be expressed as hadronic contributions in the diagrammatic notation. They will be necessary to obtain the correct critical scaling at the chiral phase transition temperature in the chiral limit.

Results for the QCD phase diagram for $N_F = 2 + 1$ from [32]

At the end of this section we want to repeat some of the results from [32], which are closely related to our work. Therefore we focus only on the $N_f = 2 + 1$ unquenched QCD part. In Fig.2.5 we give their results for the regularized condensate, where the authors find good agreement with lattice predictions below and at the crossover, but differ above the continuous transition. They attribute this discrepancy to the fixed vertex strength parameter d_1. We exploit the difference in the regularized condensate to obtain a model for d_1 in the next chapter.

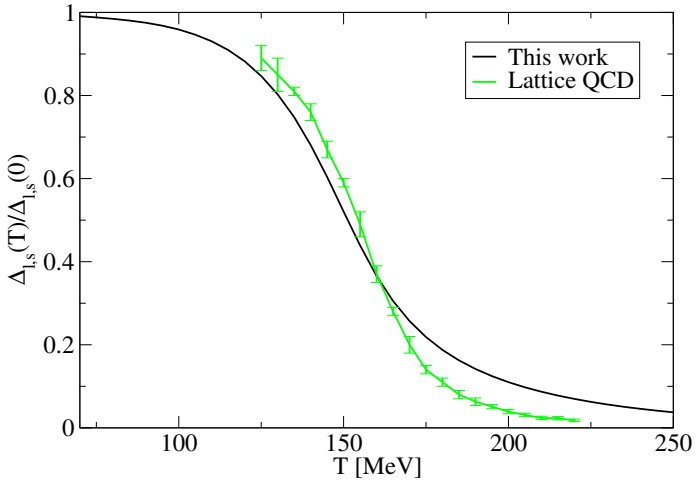

Figure 2.5: Comparison of the regularized condensate calculated in [32] to lattice results from [36] at zero chemical potential.

The major result of [32] is shown in Fig.2.6, where we see their prediction for the QCD phase diagram obtained from unquenched $N_f = 2+1$ calculations. The authors find a critical end point at μ=190 MeV and T=100 MeV. The curvature obtained from the chiral transition line is much larger than the lattice prediction. One for our work important observation is the prediction of slightly different crossover temperatures for the chiral and the deconfinement transition at zero chemical potential.

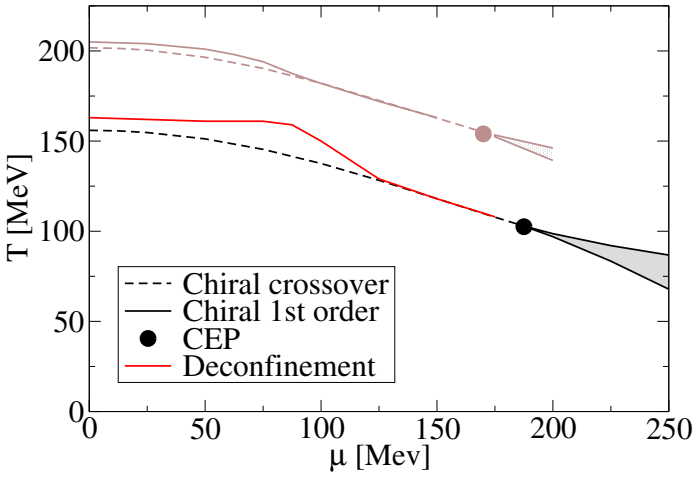

Figure 2.6: Phase diagram for $N_f = 2 + 1$ obtained in [32].

2.4 Hard thermal loops

At high temperatures T where all masses are negligible and for weak coupling g, Braaten and Pisarski first investigated the application of a method called Hard thermal loops with the involved resummation to QCD (see [8–10]). In this scenario, the fields have an effective mass of order gT and therefore it is important to distinguish between hard and soft momenta. A momentum is called *soft* if all its components are proportional to gT and called *hard* if the momentum is of order T. In case of a hard external momentum perturbative corrections to a certain diagram are suppressed by at least one power of g. In contrast, all external momenta p are soft, some loop corrections with hard internal momenta, which are proportional to $\frac{g^2T^2}{p^2}$ are as important as the tree-level diagrams. These corrections are the so called hard thermal loops due to the hard momentum in the loop calculation. As shown in [10] one can calculate the gluon self energy in the HTL limit, denoted as $\Pi^{HTL}_{\mu\nu}$. The exact calculations can be found in [35] and we find contributions from the gluon loop, the quark loop and the four gluon-vertex diagram. Using the DSE for the gluon, one can define an HTL-effective gluon propagator as

$$\left(D^{HTL}\right)^{-1}_{\mu\nu}(p) = p^2 g_{\mu\nu} - p_\mu p_\nu + \Pi^{HTL}_{\mu\nu} \tag{2.23}$$

and an equivalent expression for the HTL effective quark propagator as well as for the vertices. In order to calculate any kind of loop contribution, propagators and vertices need to be taken as the HTL effective ones where the loop momentum is soft, and as the bare propagators for hard momenta. One can use the HTL limit to define an effective theory with effective Lagrangians (see [35]). We want to emphasize that the self-energy of the gluon takes also the quark loop into account. Even if one only deals with the bare quark, this will have some sort of unquenching effects. Therefore

it is interesting to see if calculations within our unquenched system of coupled quark and gluon DSEs reveal the same behavior as the HTL method predicts.
Three attributes of hard thermal loops are mentioned in Ref. [10] and repeated here due to their importance:

- They only arise from one-loop subdiagrams
- They are gauge invariant
- They satisfy Ward identities.

Explicit calculations of the HTL-effective quark propagator can be found in [11]. Decomposed in quark and antiquark part it reads with four momentum $p = (\omega_n, \mathbf{p})$

$$S^{HTL}(p) = \frac{1}{D_+(p)} \frac{\gamma_0 + i\boldsymbol{\gamma} \cdot \mathbf{p}}{2|\mathbf{p}|} + \frac{1}{D_-(p)} \frac{\gamma_0 - i\boldsymbol{\gamma} \cdot \mathbf{p}}{2|\mathbf{p}|}, \tag{2.24}$$

where we used the γ-matrices convention (2.14). The separated inverse propagators $D_\pm(p)$ including the HTL-effective action are

$$D_\pm(p) = -ip_0 \pm |\mathbf{p}| + \frac{m_T^2}{|\mathbf{p}|} \cdot \left[Q_0 \left(\frac{ip_0}{|\mathbf{p}|} \right) \mp Q_1 \left(\frac{ip_0}{|\mathbf{p}|} \right) \right], \tag{2.25}$$

with the Legendre functions of the second kind $Q_0(x)$ and $Q_1(x)$ and the thermal mass m_T. The general relation

$$Disc \left[\frac{1}{D_\pm(p)} \right] = i\rho_\pm(\omega, |\mathbf{p}|) \tag{2.26}$$

defines the spectral densities, where $\omega = ip_0$ is the analytic continuation to a continuous Minkowski energy. The exact prediction for the spectral functions in the HTL scheme reads

$$\begin{aligned} \rho_\pm(\omega, |\mathbf{p}|) = 2\pi \frac{\omega^2 - |\mathbf{p}|^2}{2m_T^2} \left[\delta(\omega - \omega_\pm) + \delta(\omega + \omega_\mp) \right] \\ + \rho^\pm_{\text{branch cut}}, \end{aligned} \tag{2.27}$$

where $\rho^\pm_{\text{branch cut}}$ results from the existence of a branch cut in the HTL effective quark propagator below the lightcone. This branch cut originates from Landau damping, where one particle is emitted from the medium and another one is absorbed. The spectral contribution from this branch cut reads

$$\begin{aligned} \rho^\pm_{\text{branch cut}}(\omega, |\mathbf{p}|) = \frac{\pi \cdot m_T^2}{|\mathbf{p}|} \cdot (1 \mp x) \cdot \Theta(1 - x^2) \\ \times \left[|\mathbf{p}| \cdot (1 \mp x) \pm \frac{m_T^2}{2|\mathbf{p}|} \cdot \left[(1 \mp x) \cdot \ln \left(\frac{1+x}{1-x} \right) \pm 2 \right]^2 + \frac{\pi^2 m_T^4}{4|\mathbf{p}|^2} \cdot (1 \mp x)^2 \right]^{-1}, \end{aligned} \tag{2.28}$$

with the variable x defined as $x = \frac{\omega}{|\mathbf{p}|}$. This spectral density generates a basically flat contribution in the space like region.

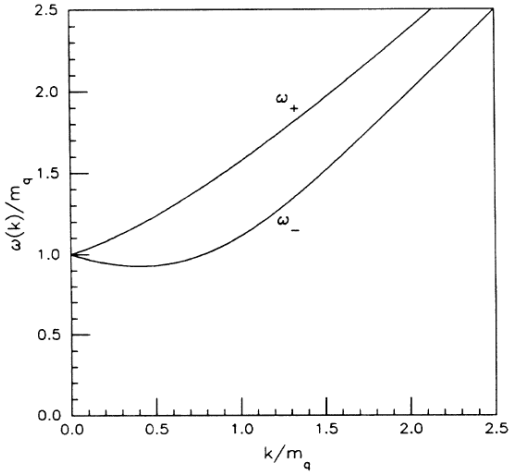

Figure 2.7: HTL prediction for the dispersion relations extracted from the effective quark propagator Eq.(2.24), taken from [11] .

In [37] we find the HTL predictions for the dispersion relations of the excitations in the spectral functions. This is also shown in Fig.2.7, where the energy and the momentum are normalized to the thermal quark mass. The behavior for small momenta as predicted in the HTL scheme for the dispersion relations is

$$\begin{aligned} E_1(|\mathbf{p}|) &\approx m_T + \frac{|\mathbf{p}|}{3} \\ E_2(|\mathbf{p}|) &\approx m_T - \frac{|\mathbf{p}|}{3} \end{aligned} \tag{2.29}$$

and for the relative spectral strength of the lower branch

$$\frac{Z_2}{Z_1 + Z_2} \approx \frac{1}{2} - \frac{|\mathbf{p}|}{3m_T}. \tag{2.30}$$

Here the second (lower) branch, with the dispersion relation $E_2(|\mathbf{p}|)$, is a collective fermionic excitation. This appears due to the introduction of the heat bath and has a helicity over chirality ratio of -1 indicating an antiparticle. Due to this antiparticle-like attribute and a antiparticle-like dispersion relation for small $|\mathbf{p}|$, it is dubbed antiquark hole or plasmino, derived from a similar phenomenon in QED plasmas, the plasmon.

2.5 Spectral functions at finite temperature

For the quark propagator in imaginary time formalism analyticity enables us to write down a spectral representation, denoted as

$$S(i\omega_n, \mathbf{p}) = \int_{-\infty}^{\infty} \frac{\mathrm{d}\omega}{2\pi} \frac{\rho(\omega, \mathbf{p})}{i\omega_n - \omega}. \tag{2.31}$$

The quark correlator, as a quantity describing a fermion, has Dirac structure. Therefore the spectral function ρ, at zero chemical potential, can be split up as

$$\rho(\omega, \mathbf{p}) = 2\pi \left(\rho_4(\omega, |\mathbf{p}|) \cdot \gamma_4 + \rho_v(\omega, |\mathbf{p}|) \cdot \frac{i\boldsymbol{\gamma} \cdot \mathbf{p}}{|\mathbf{p}|} - \rho_s(\omega, |\mathbf{p}|) \right), \tag{2.32}$$

where the conventions settled in Eq.(2.14) are used and we call ρ_4, ρ_v and ρ_s dressing functions of the spectral representation where "v" indicates the vector, "s" the scalar and "4" the Matsubara part. By comparing Eq.(2.32) with the definition of the quark propagator, Eq.(2.16), the connection between the two sets of dressing functions is apparent. As mentioned in Ref. [33], if one assumes the Fock space of our interacting theory to be positive definite, the dressing functions in Eq.(2.32) obey

$$\rho_4(\omega, |\mathbf{p}|) \geq \sqrt{\rho_v^2(\omega, |\mathbf{p}|) + \rho_s^2(\omega, |\mathbf{p}|)} \geq 0 \tag{2.33}$$

and furthermore follow the sum rules

$$\begin{aligned} 1 &= Z_2^W \int_{-\infty}^{\infty} \mathrm{d}\omega \ \rho_4(\omega, \mathbf{p}) \\ 0 &= \int_{-\infty}^{\infty} \mathrm{d}\omega \ \rho_v(\omega, \mathbf{p}) \\ 0 &= \int_{-\infty}^{\infty} \mathrm{d}\omega \ \rho_s(\omega, \mathbf{p}) \end{aligned} \tag{2.34}$$

where Z_2^W is the wave function renormalization constant. It is convenient and instructive to consider projections onto the quark and the antiquark space for vanishing momenta and the chirally restored phase, respectively. These two cases will be investigated in the following subsections.

Zero momentum

One defines the zero momentum projectors as

$$L_{\pm} = \frac{1}{2}(1 \mp \gamma_4) \tag{2.35}$$

for the quark(+) and the antiquark(-). In consequence, the spectral function for vanishing momenta can be written as

$$\rho(\omega, \mathbf{0}) = \rho^z(\omega) = \rho^z_+(\omega) L_+ \gamma_4 + \rho^z_-(\omega) L_- \gamma_4, \tag{2.36}$$

and the propagator then follows as

$$S(i\omega_n, \mathbf{0}) = S^z_+(i\omega_n) L_+ \gamma_4 + S^z_-(i\omega_n) L_- \gamma_4. \tag{2.37}$$

This means

$$\rho^z_\pm(\omega) = 2\pi \left(\rho_4(\omega, |\mathbf{0}|) \pm \rho_s(\omega, |\mathbf{0}|)\right), \tag{2.38}$$

and

$$\rho_v(\omega, |\mathbf{0}|) = 0. \tag{2.39}$$

From the spectral representation we derive the scalar relation

$$S^z_\pm(i\omega_n) = \int_{-\infty}^{\infty} \frac{\mathrm{d}\omega}{2\pi} \frac{\rho^z_\pm(\omega)}{i\omega_n - \omega}. \tag{2.40}$$

and the normalization

$$\int_{-\infty}^{\infty} \mathrm{d}\omega \ \rho^z_\pm(\omega) = \frac{2\pi}{Z_2^W} \tag{2.41}$$

from Eq.(2.34). We infere from Eq.(2.33) that $\rho^z_\pm(\omega)$ is positive semi-definite. Finally, by employing the projectors Eq.(2.35) to the propagator in the Dyson-Schwinger framework Eq.(2.16), we find the left hand side of Eq.(2.40) in our scheme denoted as

$$S^z_\pm(i\omega_n) = -\frac{i\omega_n C(i\omega_n, |\mathbf{0}|) \pm B(i\omega_n, |\mathbf{0}|)}{\omega_n^2 C^2(i\omega_n, |\mathbf{0}|) \pm B^2(i\omega_n, |\mathbf{0}|)}. \tag{2.42}$$

Chirally symmetric phase

In the case of a chirally symmetric phase with $B(i\omega_n, |\mathbf{p}|) = 0$ and therefore $\rho_s(\omega, |\mathbf{p}|) = 0$ one defines the projectors

$$P_\pm(\mathbf{p}) = \frac{1}{2}\left(1 \mp i\gamma_4 \frac{\boldsymbol{\gamma} \cdot \mathbf{p}}{|\mathbf{p}|}\right) \tag{2.43}$$

which can be understood as energy projectors for massless modes. The indication of quark and antiquark part are as in the previous subsection. Again the spectral function can be split up in terms of the projectors as

$$\rho(\omega, \mathbf{p}) = \rho^p_+(\omega) P_+ \gamma_4 + \rho^p_-(\omega) P_- \gamma_4 \tag{2.44}$$

and the propagator as

$$S(i\omega_n, \mathbf{p}) = S_+^p(i\omega_n)P_+\gamma_4 + S_-^p(i\omega_n)P_-\gamma_4. \tag{2.45}$$

While we find

$$\rho_\pm^p(\omega, |\mathbf{p}|) = 2\pi \left(\rho_4(\omega, |\mathbf{p}|) \pm \rho_v(\omega, |\mathbf{p}|)\right). \tag{2.46}$$

the normalization of $\rho_\pm^p(\omega, |\mathbf{p}|)$ is the same as in Eq.(2.41) and we encounter a similar (scalar) relation from the spectral representation

$$S_\pm^p(i\omega_n, |\mathbf{p}|) = \int_{-\infty}^{\infty} \frac{\mathrm{d}\omega}{2\pi} \frac{\rho_\pm^p(\omega, |\mathbf{p}|)}{i\omega_n - \omega}. \tag{2.47}$$

We can derive the according propagator in our framework, as in the previous case, by employing the projectors Eq.(2.43) to the quark propagator Eq.(2.16), leading to

$$S_\pm^p(i\omega_n, |\mathbf{p}|) = -\frac{i\omega_n C(i\omega_n, |\mathbf{p}|) \pm |\mathbf{p}| A(i\omega_n, |\mathbf{p}|)}{\omega_n^2 C^2(i\omega_n, |\mathbf{p}|) \pm |\mathbf{p}|^2 A^2(i\omega_n, |\mathbf{p}|)}. \tag{2.48}$$

2.6 Schwinger function

Another quantity of interest is the Schwinger function $S_+^M(\tau)$, which is the Fourier transform of the propagator $S_+^M(i\omega_n)$ as defined in Eq.(2.11) at $|\mathbf{p}| = 0$:

$$S_+^M(\tau) = T \cdot \sum_n e^{-i\omega_n \tau} S_+^M(i\omega_n). \tag{2.49}$$

At zero temperature the Schwinger function is a tool to investigate positivity violations in the quark propagator. From charge conjugation invariance we find the symmetry

$$S_\pm^M(\tau) = S_\mp^M(1/T - \tau). \tag{2.50}$$

In the phase of chiral symmetry restoration in the chiral limit

$$S_+^M(\tau) = S_+^M(1/T - \tau) \tag{2.51}$$

is given due to $B(\mathrm{i}\omega_n,0)=0$ and we also find $S_+^M(i\omega_n) = -S_+^M(-i\omega_n)$ (compare [33]). In Ref. [2], two important relations for the Schwinger function at finite temperature are given.

1. The connection to the calculated spectral density is

$$S_+^M(\tau) = \int \frac{d\omega}{2\pi} \rho_+^M(\omega) \cdot \frac{e^{(1/2-\tau T)\omega/T}}{e^{\omega/2T} + e^{-\omega/2T}}. \tag{2.52}$$

   This means that a positive spectral function always implies a positive Schwinger function. A negative Schwinger function, or positivity violation, corresponding to a negative spectral function, leads to the absence of the according particles from physical space, implying the phenomenon of confinement.

2. The second relation connects the search for positivity violations in the spectral function with the curvature of the logarithm of the Schwinger function:

$$\rho_+^M(\omega) \geq 0 \Rightarrow \frac{\partial^2 S_+^M(\tau)}{\partial \tau^2} \geq 0 \tag{2.53}$$

This shows that a concave curvature of the logarithm of the Schwinger function implies positivity violations in the spectral function and therefore can be interpreted as an indicator for confinement.

3 Numerical setup and approaches to the spectral function

After setting the theoretical foundation of finite temperature QCD we turn to the details of the numerical calculation. We introduce the Levenberg-Marquardt method as a fitting routine for multiple parameters and explain its general idea. The following section deals with the details for solving the Dyson-Schwinger equation focusing in particular on the vertex strength parameter d_1 above the phase transitions for the considered scenarios and a comparison of quenched and unquenched propagators. We then briefly address some more details of the fitting routine and introduce the ansätze for the spectral functions.

3.1 Levenberg-Marquardt Method

In order to perform a nonlinear multiparametrical fit, one needs an appropriate fitting routine. The Levenberg-Marquardt method is an advanced fitting routine with all necessary features. The fitting process is translated into the task of minimizing a predefined merit function $\chi^2(\mathbf{a})$ with $\mathbf{a}$ being the set of N parameters to vary. A properly defined merit function will show approximately quadratic behavior close to a minimum (see [38]):

$$\chi^2 \approx \gamma - \mathbf{d} \cdot \mathbf{a} + \frac{1}{2} \cdot \mathbf{a} \cdot \underline{D} \cdot \mathbf{a}. \tag{3.1}$$

Here $\mathbf{d}$ is a vector of size N and $\underline{D}$ is proportional to the NxN curvature matrix (compare Eq.(3.4)). In this case one knows from minimization techniques how to calculate the next set of parameters $\mathbf{a}_{new}$ from the old set $\mathbf{a}_{old}$

$$\mathbf{a}_{new} = \mathbf{a}_{old} + \underline{D}^{-1} \cdot \left[-\nabla \chi^2(\mathbf{a}_{old}) \right]. \tag{3.2}$$

In case the approximation with the current set of parameters $\mathbf{a}$ is rather poor, one can, according to the steepest descent method (compare Ref. [38]), take one step down the gradient

$$\mathbf{a}_{new} = \mathbf{a}_{old} - c \cdot \nabla \chi^2(\mathbf{a}_{old}). \tag{3.3}$$

For the minimization process one defines

$$\alpha_{kl} = 2 \cdot \underline{D} = \frac{1}{2} \frac{\partial^2 \chi^2}{\partial a_k \partial a_l} \tag{3.4}$$

and

$$\beta_k = -\frac{1}{2}\frac{\partial \chi^2}{\partial a_k}. \tag{3.5}$$

The figure of merit is usually defined as

$$\frac{\chi^2}{\text{d.o.f.}} = \frac{1}{N_{data} - N} \cdot \sum_i^{N_{data}} \frac{[y_i - y(x_i; \mathbf{a})]^2}{\sigma_i^2} \tag{3.6}$$

where $y(x; \mathbf{a})$ is the model function one wants to fit to the data (x_i, y_i) and d.o.f. stands for degrees of freedom. Using also the first partial derivatives we find

$$\alpha_{kl} = \sum_{i=1}^{N_{data}} \frac{1}{\sigma_i^2} \left[\left.\frac{\partial y(x; \mathbf{a})}{\partial a_k}\right|_{x=x_i} \cdot \left.\frac{\partial y(x; \mathbf{a})}{\partial a_l}\right|_{x=x_i} \right] \tag{3.7}$$

$$\beta_k = \sum_{i=1}^{N_{data}} \frac{[y_i - y(x_i; \mathbf{a})]}{\sigma_i^2} \left.\frac{\partial y(x, \mathbf{a})}{\partial a_k}\right|_{x=x_i}. \tag{3.8}$$

Second order partial derivatives are neglected since the form of their appearance shows that they would cause more disadvantages due to destabilizing effects than improve the routine.

Eqs.(3.2) and (3.3) can now be rewritten and combined to the central equation of the Levenberg-Marquardt method

$$\sum_{l=1}^{N} \alpha'_{kl} \cdot \delta a_l = \beta_k \tag{3.9}$$

where

$$\delta a_l = (\mathbf{a}_{new} - \mathbf{a}_{old})_l \tag{3.10}$$

and

$$\alpha'_{jj} = \alpha_{ll} \cdot (1 + \lambda)$$
$$\alpha'_{kl} = \alpha_{kl} \text{ , for } k \neq l.$$

The appearance of the parameter λ is connected to the constant c in Eq.(3.3) and some general considerations. λ basically switches smoothly between the quadratic approximation Eq.(3.1) and the steepest descent method Eq.(3.3). One starts with a set of parameters $\mathbf{a}_{old}$ and a value for λ. The linear equations (3.9) are solved for δa_l and the trial parameters $\mathbf{a}_{new}$ are calculated. If $\chi^2(\mathbf{a}_{new})$ is smaller than the old value, λ is divided by a factor α which is equivalent to get closer to the quadratic approximation. The routine stops when the difference between the old and the new value of the merit function is smaller than a defined limit. If the value of the merit function is bigger than the old one, λ is multiplied by α and one goes back to $\mathbf{a}_{old}$ to start over. Increasing λ makes the matrix α'_{kl} diagonal-dominant which is the same as using the steepest descent method to go one step down the gradient.

3.2 The quark propagator and models for the vertex strength parameter

The quark propagator in Matsubara formalism calculated in the DSE approach, as defined in Eq.(2.16), is the main input for our investigations. For the calculation of the quark propagators we apply the code used in [32] written by Jan Lücker. The theoretical background as well as the truncation scheme have been already discussed in chapter 2. In this section we address the remaining open questions and some details of the calculation.
In both, the quenched and in the unquenched calculations a O(4) cutoff of the form

$$\omega_n^2 + |\mathbf{p}|^2 = \Lambda^2 \tag{3.11}$$

is applied, leading to different momentum grids for each Matsubara frequency. The cutoff dependence is removed by a renormalization at $|\boldsymbol{\mu}| = 80\text{GeV}$ with a MOM scheme, satisfying

$$\begin{aligned} B(i\omega_0, \boldsymbol{\mu}) &= m(|\boldsymbol{\mu}|) = m_0, \\ C(i\omega_0, \boldsymbol{\mu}) &= 1. \end{aligned} \tag{3.12}$$

The strange quark mass in the $N_f = 2 + 1$ unquenched calculations is set to $m_s = 54$ MeV. Our set of truncated Dyson-Schwinger equations is solved numerically by iteration, resulting in the dressing functions of the quark propagator for ω_{-N} to ω_{N-1} with $N = 5$. We also obtain the wave function renormalization constant,

$$Z_2^W \lesssim 1 \tag{3.13}$$

from all our calculations.

As mentioned in the previous chapter, the quenched gluon propagator in Landau gauge is fitted to lattice calculations [39], which are available for certain temperatures. Therefore one has to develop a method to derive the gluon dressing functions (propagator) for any temperature of interest. We used two ansätze to resolve this issue:

1. **Linear interpolation:** If one is interested in quark propagators in a temperature regime, where the fits of the dressing functions to the lattice data are available, an interpolation of the dressing functions in T is possible. We employ a linear interpolation to follow [33].

2. **Quadratic fit:** The main instrument used to derive the gluon dressing functions in our work is a quadratic fit to those gluon dressing functions, derived from the lattice gluon propagators.

If not otherwise indicated we use the quadratic fit method. The linear interpolation is only considered in the quenched scenario for comparison with [33]. The values for the gluon dressing functions for both schemes differ little for temperatures up to $T \approx 450$ MeV.

Vertex strength parameter d_1

An open question is the value of the strength parameter d_1 in the ansatz for the quark-gluon vertex Eq.(2.22) above the particular phase transition. The strategy in the quenched as well as in the unquenched case is to extract certain quantities from our calculations and vary the vertex strength until we achieve satisfying agreement with lattice results.

- **Quenched QCD:** In the second chapter we found a first order phase transition for the case of quenched QCD in the Columbia plot Fig.2.1. This transition happens at $T_{que}^{1st} \approx 277$ MeV, independent of the quark mass. We consider two cases for the parameter d_1 resulting from the two methods to obtain the gluon dressing functions at various temperatures. In case of linear interpolation we adapt the investigated temperatures and the values for d_1 used in [33] in order to compare our findings with their results. The idea is to fix the values for d_1 by comparing the obtained with the thermal quark mass from lattice calculations [16]. The particular values together with our results for thermal masses and those of [33] are shown in Table I in chapter 4.
  However, the fitted gluon dressing functions differ to those dressing functions obtained via linear interpolation leading to different vertex strength parameters. We adapted the idea of comparing to the lattice results for the thermal mass from [16] and obtained the following ansatz for the parameter above the critical temperature of $T_{que}^{1st} = 277$ MeV:

$$d_1^{que}(T) = 0.560 \cdot \left(\frac{T_{que}^{1st}}{T}\right)^{1.057} \text{GeV}^2. \tag{3.14}$$

  The resulting thermal masses as well as the temperatures and exact values used for d_1 are listed in Table II. One important feature of the model Eq.(3.14) is the possibility to calculate the vertex strength parameter at arbitrary temperatures. One additional remark on the lattice data for the thermal mass is, that by comparing with [17] one sees the thermal masses have been updated recently and the values seem to be lower. This suggests an even smaller vertex strength as modeled in Eq.(3.14), but it will be left for future investigations to explore the lowering of the vertex strength, when there is also more input for the gluon propagator available.

- **Unquenched QCD - physical masses:** For the unquenched case there is no lattice data for the thermal mass, as used to fix d_1 in the quenched case, available. In the case of physical quark masses with $m_{u,d} = 2$ MeV we used the results from [32] for the chiral condensate shown in Fig. 2.5. We already discussed briefly that above the crossover the results do not quite match the lattice prediction. The vertex strength parameter was varied to roughly fit the results in our Dyson-Schwinger scheme to the lattice values of the regularized condensate. We obtained an adapted vertex strength, once again following a power law

$$d_1^{unq,phys}(T) = 7.67 \cdot \left(\frac{T_{unq,phys}^{cross}}{T} \right)^{0.966} \text{ GeV}^2 \tag{3.15}$$

  with $T_{unq,phys}^{cross} \approx 156$ MeV. However this model will only be reliable up to the critical temperature of the quenched phase transition T_{que}^{1st}. At this temperature we will see (artificial) residual effects from the quenched case. By looking at Fig.2.4 and Eq.(2.22) we remember, the unquenching was done by merely adding the quark loop leaving the inner structure of the quenched gluon part unchanged. As discussed in chapter 2 unquenching effects are expected in the Yang-Mills part of the gluon as well as in the vertex.

- **Unquenched QCD - chiral limit:** As mentioned in the consideration of the Columbia plot in section 2.1, we expect to find a second order phase transition with a critical temperature $T_{unq,chiral}^{2nd}$. In the case of unquenched QCD in the chiral limit we have no lattice data available, since calculations of the quark propagator are impossible for this scenario. However, we assume the vertex strength to decrease as in the two previous cases. Motivated by the behavior of roughly $\frac{1}{T}$ we propose a model for the vertex strength reproducing $d_1 = 7.5$ GeV^2 right before the phase transition:

$$d_1(T) = 7.5 \cdot \frac{T_{unq,chiral}^{2nd}}{T} \text{ GeV}^2. \tag{3.16}$$

  In order to test the setup concerning the dependence of the vertex strength a second model is applied keeping the vertex strength parameter to the constant value defined before

$$d_1(T) = 7.5 \text{ GeV}^2. \tag{3.17}$$

  This certainly gives simply an impression about the impact of d_1 rather than realistic results, since we expect the vertex strength to decrease eventually.

Comparison of quenched and unquenched quark propagator

At the end of this section we want to compare the quenched and unquenched quark propagators by investigating their dressing functions (see Eq.(2.16)). In Figures 3.1a

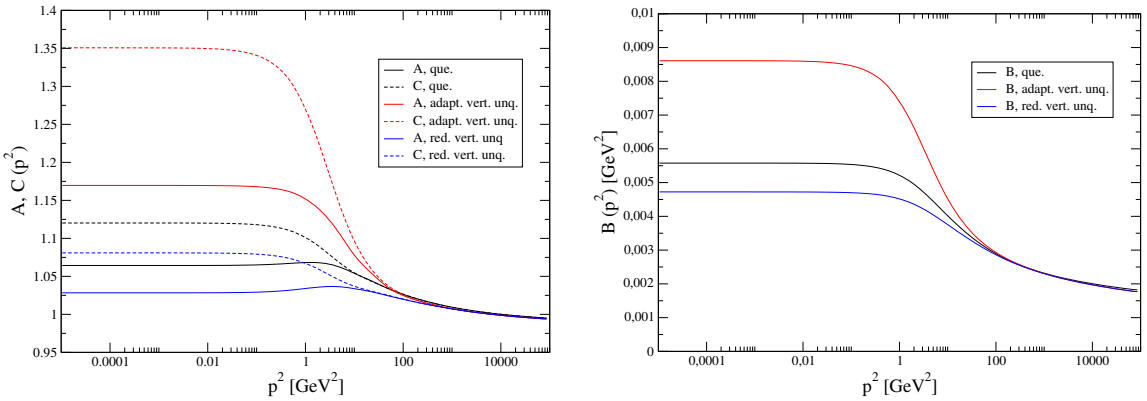

(a) Vector dressing functions

(b) Scalar dressing function

Figure 3.1: Comparison of the vector and scalar dressing functions for quenched and unquenched propagators at T=346.25 MeV and m_0=2 MeV.

and 3.1b the dressing functions at T=346.25 MeV and m_0=2 MeV are shown for the first Matsubara mode ω_0. The quenched case is represented by black lines, while the red and the blue lines correspond to the unquenched scenario, for a vertex strength parameter $d_1 = 3.55$ GeV^2, calculated with Eq.(3.15), and a tenth of this value respectively. We use two values for d_1 in the calculation of the unquenched quark propagator to estimate the influence of the vertex strength.
While the shape of the dressing functions B and C shows no dependence on the parameter d_1, there appears a maximum in the A dressing function for $d_1 = 0.355$ GeV^2 while the vector dressing function for the larger value of d_1 behaves linear until it eventually decreases. It is striking that the shape of the quenched and the unquenched dressing function with smaller d_1 is similar. This is due to the structure of the quark-gluon vertex Eq.(2.22). Since the parameter d_1 appears quadratic in backcoupling processes from the unquenched Yang-Mills sector, leading to a suppression of the unquenching effects for values of d_1 smaller than one. On the other hand the backcoupling effects are enhanced for values of d_1 larger than one. While the values for the unquenched dressing functions with the smaller (reduced) parameter d_1 and those in the quenched case are comparable, the unquenched propagator with $d_1 = 3.55$ GeV^2 displays larger values for all dressing functions.
In Fig.3.2 we compare the dressing functions in the same setup but with $d_1 = 1$ GeV^2 in both calculations to see the pure unquenching effects. We observe that the unquenching is reflected in a lowering of all dressing functions. While the shapes of the functions B and C are similar, we find again a maximum in the vector dressing function A for the unquenched case.

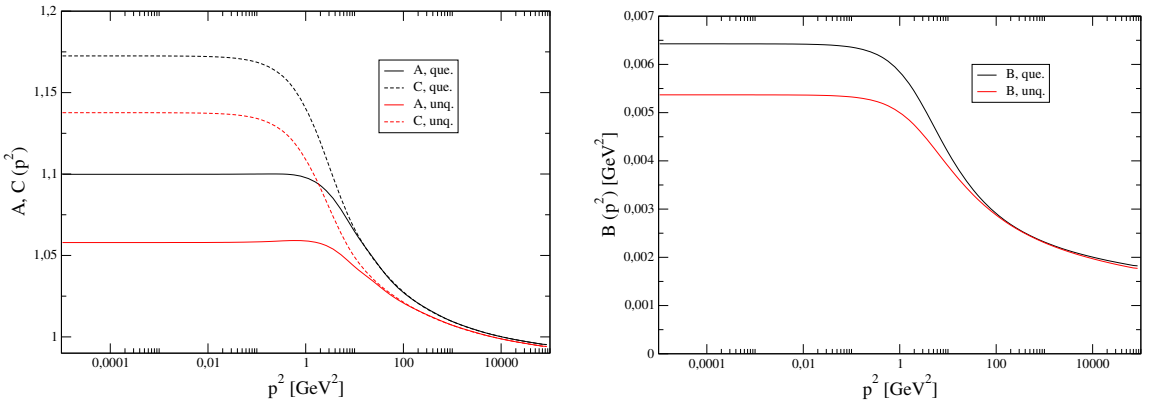

(a) Vector dressing functions

(b) Scalar dressing function

Figure 3.2: Comparison of the vector and scalar dressing functions for quenched and unquenched propagators at T=346.25 MeV, m_0=2 MeV and d_1 = 1 GeV^2.

3.3 Fitting strategy

The process of fitting the spectral function to the quark propagator is realized in a *C++* program which needs the dressing functions of the quark propagator as input. Those propagators are obtained by the previously mentioned program. Partially based on source codes from [38] the Levenberg-Marquardt method is used to fit the integral of a chosen spectral function to the quark two-point function. We want to emphasize that the quark spectral function refers to the spectral functions ρ^+.
The model function in the Levenberg-Marquardt method is one (or the combination) of the propagator $S^{\pm}(i\omega_n, |\mathbf{p}|)$, calculated from the ansätze for the spectral function, which will be introduced in the next section. Generally, the figure of merit is defined as in Eq.(3.6). In our case we assume uncorrelated data and set $\sigma_i = 1$ for all data points. To distinguish this from the previous figure of merit we define

$$\frac{l^2_{\pm}(|\mathbf{p}|)}{\text{d.o.f.}} = \frac{1}{N_{data} - N} \cdot \sum_{i}^{N_{Matsubara}} |S^{\pm,DSE}(|\mathbf{p}|, \omega_i) - S^{\pm,Fit}(|\mathbf{p}|, \omega_i)|^2. \tag{3.18}$$

Since we always calculate this figure of merit we will use $\frac{l^2}{\text{d.o.f.}}$ and l^2 equivalently. We fit the quark propagator for every $|\mathbf{p}|$ separately. Remembering that we use a O(4)-cutoff for the production of the data, an interpolation is necessary to set the propagator for every Matsubara frequency on the same momentum grid. For this process an interpolation with cubic splines is used (compare [38]). Another necessary tool is some sort of numerical integration. Here we decided to use the Gauss-Legendre integration due to its numerical stability and divided the region of integration in small

intervals to keep the order of the used polynomials as low as possible. All results which needed usage of this numerical integration are checked to be independent of an increase of the integration parameters. For more details on the Gauss-Legendre integration see [38].
For the fitprocess the factor α is set to 15, ensuring a moderate transition between a quadratic approximation of l^2 and the steepest descent method. The fitroutine stops when the the difference between the new and the old value for l^2 falls below a particular value for the second time. This value depends on the current setup and fitfunction.
Since we calculate the quark propagators for ω_{-N} to ω_{N-1} with $N = 5$ and we need a higher number of Matsubara frequencies, we use a extrapolation method based on the isotropic behavior of the quark dressing functions at high momenta. The Euclidean four momentum squared can be rewritten as

$$\begin{aligned} p^2 &= \omega_n^2 + |\mathbf{p}|^2 \\ &= \omega_{max}^2 + \underbrace{\left(\omega_n^2 - \omega_{max}^2 + |\mathbf{p}|^2\right)}_{:=|\mathbf{p}'|^2}. \end{aligned} \tag{3.19}$$

As indicated in Eq.(3.19), we define the absolute value of the new three momentum $|\mathbf{p}'|$ and now extrapolate the quark dressing functions

$$X(\omega_n, |\mathbf{p}|) \in \{A(\omega_n, |\mathbf{p}|), B(\omega_n, |\mathbf{p}|), C(\omega_n, |\mathbf{p}|)\}$$

for n > max.

$$X(\omega_n, |\mathbf{p}|) = X(\omega_{max}, |\mathbf{p}'|). \tag{3.20}$$

In order to extrapolate to higher Matsubara frequencies the O(4) cutoff has to be set accordingly. As it turns out, it is sufficient in all cases to extrapolate to max=70, leaving us with 140 data points for the Matsubara frequencies. We want to mention that the numerical calculation of the unquenched propagator turns out to be sensitive to the number of accounted Matsubara frequencies. Therefore we chose to calculate the propagators with N=5 to stay in one line with [32].

3.4 Ansätze for the spectral function

In this section we present the different ansätze for the spectral function $\rho^{\pm}(\omega, |\mathbf{p}|)$ as introduced in Eqs.(2.38) and (2.46). We still carry the signs for both, the quark and the antiquark spectral function even if we are only interested in the quark spectral functions.

HTL: Two-pole plus continuum

From our discussion of the HTL results we infer one appropriate ansatz for the spectral function is the HTL suggested two-pole ansatz plus continuum shown in

Eq.(2.27). The simple cornerstone for the HTL ansatz is a pole in the spectral density

$$\rho^{\pm}_{\text{pole}}(\omega, |\mathbf{p}|) = 2\pi \cdot Z(|\mathbf{p}|) \cdot \delta(\omega \mp E(|\mathbf{p}|)). \tag{3.21}$$

The fit parameters are momentum dependent and contain the dispersion relation for the pole-particle. As already discussed, the HTL formalism predicts two poles, the quark-like pole and the so called plasmino pole. The plasmino can be understood as a collective excitation showing antiparticle-like evolution at small momenta in the dispersion relation. The spectral density for two poles reads

$$\begin{aligned}\rho^{\pm}_{\text{two-pole}}(\omega, |\mathbf{p}|) &= \rho^{\pm}_{\text{pole }1}(\omega, |\mathbf{p}|) + \rho^{\mp}_{\text{pole }2}(\omega, |\mathbf{p}|) \\ &= 2\pi \cdot Z_1(|\mathbf{p}|) \cdot \delta(\omega \mp E_1(|\mathbf{p}|)) + 2\pi \cdot Z_2(|\mathbf{p}|) \cdot \delta(\omega \pm E_2(|\mathbf{p}|))\end{aligned} \tag{3.22}$$

where the factor of 2π is due to the normalization of the spectral representation in Eq.(2.31) and the inversion of the $\pm$ due to the expectation of an antiparticle like behavior of the second pole.

From Eq.(3.22) it is obvious, that $\rho^{+}_{\text{two-pole}}(\omega, |\mathbf{p}|)$ and $\rho^{-}_{\text{two-pole}}(\omega, |\mathbf{p}|)$ are symmetric under exchange of parameters if the continuum contribution Eq.(2.28) is not present. What we call the HTL ansatz is the spectral density in Eq.(3.22) plus the branch cut in Eq.(2.28)

$$\rho^{\pm}_{\text{HTL}}(\omega, |\mathbf{p}|) = \rho^{\pm}_{\text{two-pole}}(\omega, |\mathbf{p}|) + \rho^{\pm}_{\text{branch cut}}(\omega, |\mathbf{p}|). \tag{3.23}$$

We remember that the Θ-function in Eq.(2.28) ensures that the continuum only contributes in the space-like region of the spectrum. The normalization of the ansatz is given by

$$\int_{-\infty}^{\infty} \mathrm{d}\omega \ \rho^{\pm}_{HTL}(\omega) = 2\pi Z_{total}(|\mathbf{p}|), \tag{3.24}$$

where the left part for the HTL spectral function is found to be

$$Z_{total}(|\mathbf{p}|) = Z_1(|\mathbf{p}|) + Z_2(|\mathbf{p}|) + \frac{1}{2\pi}\int_{-1}^{1} \mathrm{d}x \rho^{\pm}_{\text{branch cut}}(x, |\mathbf{p}|). \tag{3.25}$$

From the spectral representation for one pole Eq.(3.21), the corresponding propagator can be easily calculated and reads

$$S^{\pm}_{\text{pole}}(i\omega_n, |\mathbf{p}|) = \frac{Z(|\mathbf{p}|)}{i\omega_n \mp E(|\mathbf{p}|)}. \tag{3.26}$$

The propagator for ansatz (3.23) follows immediately.

Tripole ansatz

In reference [28] an investigation of the spectral function for the quark propagator calculated from the QCD gap equation in a Dyson-Schwinger approach with a temperature dependent vertex model was done. Using the Maximum Entropy method, a tripole solution for the chiral limit of unquenched QCD is suggested. For later studies and to test the prediction we include this ansatz in our repertoire. The systematics are just the same as for Eq.(3.22). The ansatz for the spectral function reads

$$\begin{aligned}\rho^{\pm}_{\text{Tripole}}(\omega,|\mathbf{p}|) = 2\pi\cdot Z_1(|\mathbf{p}|)\cdot\delta(\omega\mp E_1(|\mathbf{p}|)) + 2\pi\cdot Z_2(|\mathbf{p}|)\cdot\delta(\omega\pm E_2(|\mathbf{p}|)) \\ + 2\pi\cdot Z_3(|\mathbf{p}|)\cdot\delta(\omega\mp E_3(|\mathbf{p}|)),\end{aligned} \tag{3.27}$$

and the quark propagator follows again from Eq.(3.26).

Breit-Wigner function

Due to effects of a strongly interacting medium one would expect not only sharp particle poles in the spectral representation and a continuum contribution from the branch cut but also a broadening of the correlated peaks. To cover this possibility we include the Breit-Wigner function as an ansatz in our spectral function. In order to agree with the normalization for the two-pole ansatz (Eq.(3.24)), the ansatz for the Breit-Wigner function is

$$\rho^{\pm}_{\text{Breit-Wigner}}(\omega,|\mathbf{p}|) = \frac{2\cdot Z(|\mathbf{p}|)\cdot\Gamma(|\mathbf{p}|)}{\left(\omega\mp E(|\mathbf{p}|)\right)^2+\Gamma^2(|\mathbf{p}|)}. \tag{3.28}$$

leading with Eq.(2.31) to the propagator

$$\begin{aligned}S^{\pm}_{\text{Breit-Wigner}}(i\omega_n,|\mathbf{p}|) = &\frac{Z(|\mathbf{p}|)}{\mp E(|\mathbf{p}|)+i\left(\omega_n+\Gamma(|\mathbf{p}|)\right)}\cdot\Theta(\omega_n) \\ &+\frac{Z(|\mathbf{p}|)}{\mp E(|\mathbf{p}|)+i\left(\omega_n-\Gamma(|\mathbf{p}|)\right)}\cdot\Theta(-\omega_n).\end{aligned} \tag{3.29}$$

The idea is to use the Breit-Wigner ansatz to investigate whether one has a sharp pole (Γ becoming very small) or needs a broader distribution. If one replaces the poles in the HTL ansatz by Breit-Wigner functions one needs to be careful applying the HTL continuum in Eq.(2.28) since it is derived from a propagator with two poles rather than broader distributions. Therefore an ansatz with two Breit-Wigner functions is similar to the two pole ansatz and reads

$$\rho^{\pm}_{\text{2BW}}(\omega,|\mathbf{p}|) = \rho^{\pm}_{\text{BW }1}(\omega,|\mathbf{p}|) + \rho^{\mp}_{\text{BW }2}(\omega,|\mathbf{p}|). \tag{3.30}$$

A real advantage in this case is that the propagator Eq.(3.29) is given in an analytical form, excluding issues due to numerical integration during the fitting procedure.

Gauss function

In principle, there is additionally the possibility to use an ansatz with two Gaussian functions, as mentioned in Ref. [33]. However the Gaussian as an ansatz for the spectral density has a drawback due to a non-analytical solution of the integral given in Eq.(2.31). Since one has to calculate not only the propagator $S^{\pm}_{\text{Gauss}}(i\omega_n, |\mathbf{p}|)$ but also its partial derivatives with respect to the parameters, a numerical integration includes possible sources for uncertainties. After all the Gaussian has no such physical motivation as the Breit-Wigner ansatz representing a particle with a mean and a certain decay width, which is used in the investigation of spectral representations in experimental physics. Therefore we disregard the Gaussian as a possible ansatz for the spectral function.

Combinations of different fitfunctions

Since the analytical form and the input for the fitting routine was already at hand we investigated different combinations of the pole ansatz Eq.(3.21) and the Breit-Wigner ansatz Eq.(3.28). Firstly it is apparent that a Breit-Wigner function will melt down to a pole if the pole is suggested by the data. It turns out that different combinations of poles and Breit-Wigner functions are sensitive to the initial values of the parameters. One needs to distinguish carefully between two cases:

1. Dependence on initial values gives solutions with the same l^2.

2. Dependence on initial values gives solutions with different l^2.

While in the first case a redundancy of parameters leaves us with a whole family of equally suitable solutions, the second case points towards local minima in the l^2-space. In this case one has to find the global minimum by hand, which is of course a procedure that has to be used carefully.
There are three interesting examples we found to be useful throughout our investigations.

1. **HTL plus Breit-Wigner:** Firstly, there is the HTL solution plus a Breit-Wigner function. The idea is that the Breit-Wigner function simulates background and contributions from the branch cut while the two poles describe the previously seen quark and plasmino branch. The ansatz for the spectral density in this case is

$$\rho^{\pm}_{\text{HTL plus Breit-Wigner}}(\omega, |\mathbf{p}|) = \rho^{\pm}_{\text{HTL}} + \frac{2 \cdot Z_{BW}(|\mathbf{p}|) \cdot \Gamma_{BW}(|\mathbf{p}|)}{\left(\omega \mp E_{BW}(|\mathbf{p}|)\right)^2 + \Gamma^2_{BW}(|\mathbf{p}|)}. \tag{3.31}$$

2. **Pole plus Breit-Wigner:** Another ansatz we used with success for the unquenched case with physical mass, consists of one pole and one Breit-Wigner function. The spectral function then reads

$$\rho^{\pm}_{\text{Pole plus Breit-Wigner}}(\omega, |\mathbf{p}|) = 2\pi \cdot Z_1(|\mathbf{p}|) \cdot \delta(\omega \mp E_1(|\mathbf{p}|)) + \frac{2 \cdot Z_2(|\mathbf{p}|) \cdot \Gamma(|\mathbf{p}|)}{(\omega \pm E_2(|\mathbf{p}|))^2 + \Gamma^2(|\mathbf{p}|)}. \tag{3.32}$$

3. **Three Breit-Wigner functions:** Finally, we also used a very general ansatz. This was mainly important to investigate the given structure when we found one or two Breit-Wigner functions to melt down to a pole. The propagator is simply given as

$$\rho^{\pm}_{\text{Three Breit-Wigner}}(\omega, |\mathbf{p}|) = \rho^{\pm}_{\text{2BW}} + \frac{2 \cdot Z_3(|\mathbf{p}|) \cdot \Gamma_3(|\mathbf{p}|)}{(\omega \mp E_3(|\mathbf{p}|))^2 + \Gamma_3^2(|\mathbf{p}|)}. \tag{3.33}$$

4 Quark spectral functions in quenched QCD

In this chapter we present our results for the spectral functions of quenched QCD. For this scenario, where all quark loops are neglected, we expect a first order phase transition at $T_{que}^{1st} \approx 277 MeV$. To test our fitting routine, in a first step we compare our findings with the HTL ansatz in the chiral limit to those obtained in [33]. We then use our ansatz for the vertex strength parameter Eq.(3.14) to explore the spectrum for higher temperatures, with the HTL as well as with an improved spectral function including an additional Breit-Wigner function. Finally we consider the case of finite quark masses in the HTL as well as the improved ansatz.

4.1 Spectral functions in the chiral limit

In this section we draw our attention to the case of the chiral limit and therefore consider the spectral density as defined in Eq.(2.46).

Comparison with previous calculations

In order to test the fitting routine, the HTL ansatz from Eq.(3.23) is used to fit the spectral function to the calculated quenched data. The propagators have been calculated using the linearly interpolated gluon dressing functions and the values for d_1 from [33], since we want to compare our results with their findings. In Fig. 4.1a one can see the established pattern of the quark and plasmino dispersion relations. While the quark branch shows eventually the behavior of a free particle at high momenta, the plasmino dispersion relation first follows antiparticle-like behavior, reaches a minimum at about 0.4T and rises again. Since we included the HTL continuum, both branches stay time-like, which means

$$E(|\mathbf{p}|) > |\mathbf{p}| \quad \text{, for all } |\mathbf{p}|. \tag{4.1}$$

If we compare the predictions from HTL for the slope of the curves (compare Eq.(2.29) and Eq.(2.30)) we find good agreement for both, the dispersion relations and the spectral strength with the results given in [33]. The obtained values for the thermal mass are shown in Table I.

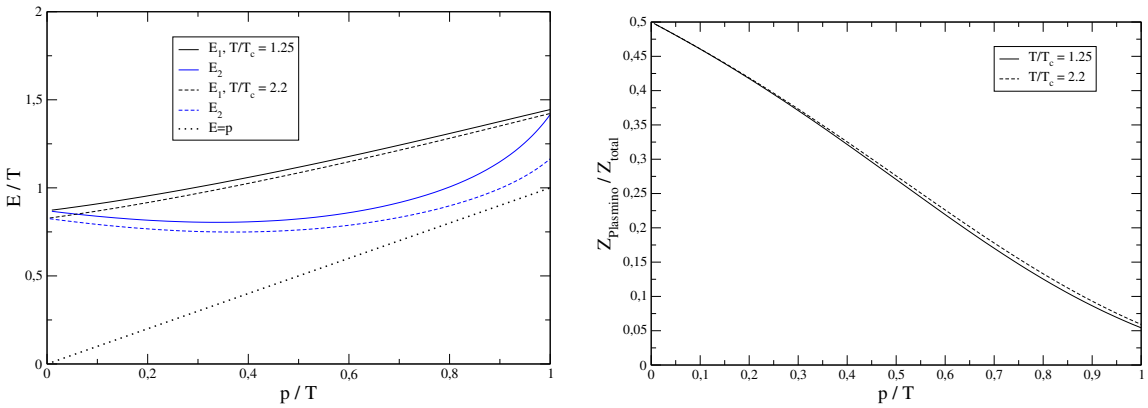

(a) Dispersion relations

(b) Relative strength of the plasmino pole

Figure 4.1: Results for the dispersion relations and spectral strength for the two-pole ansatz plus continuum in quenched QCD in the chiral limit for 1.25 T_C (solid lines) and 2.2 T_C (dashed lines) for linearly interpolated gluon dressing functions.

T/T_C	1.25	1.5	2.2
$d_1[GeV^2]$	0.5	0.4	0.25
m_T/T	0.870	0.867	0.827

Table I: Values for the strength d_1 of the quark-gluon vertex and the obtained thermal masses for the linearly interpolated gluon dressing functions

Since the comparison with [33] confirms the fact that our fitting routine works well, we next explore the situation in a different setup.

Calculations with the model vertex strength

From now on a slightly different and more advanced description of the gluon propagator for the calculation of the quark propagator is used. This is necessary to be able to extrapolate to higher temperatures. Following [32] we use the fit for the dressing functions of the gluon propagator to the lattice data, as described in chapter 3. This provides the opportunity to calculate the gluon dressing functions at higher temperatures. By changing the gluon propagator we expect the vertex strength d_1, as fixed in Table I, not to reproduce the calculated thermal masses exactly. Since we aim at providing results at higher temperatures, it is necessary to model the vertex strength parameter d_1. This model was already introduced in Eq.(3.14) in chapter 3. The first three values in Table II are the adjusted values used to fit the power law.

Firstly, we want to explore and compare the results for the HTL-suggested ansatz

T/T_C	1.25	1.5	3	4	5
$d_1[GeV^2]$	0.49	0.32	0.18	0.13	0.10
m_T/T	0.8990	0.9055	0.8753	0.8113	0.7649

Table II: Values for the strength d_1 of the quark-gluon vertex and the obtained thermal masses for the gluon dressing functions fitted to lattice results

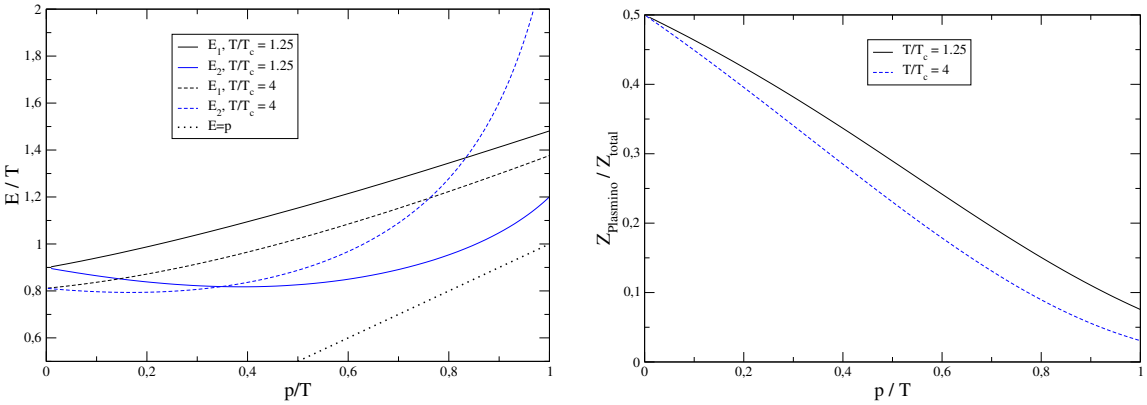

(a) Dispersion relations

(b) Relative strength of the plasmino pole

Figure 4.2: Results for the dispersion relations and spectral strength for the HTL ansatz in quenched QCD in the chiral limit for 1.25 T_C (solid lines) and 4 T_C (dashed lines) for the fitted gluon dressing functions and vertexstrength as in Table II.

in the new setup and see whether the impact is noticeable or not. In Fig.4.2 we see the dispersion relation for the two poles and the relative strength of the plasmino for 1.25 T_C and 4 T_C. We notice the shift in the thermal mass for the 1.25 T_C branches and a plasmino which is slightly steeper after the minimum in comparison with Fig.4.1. For a temperature of 4 T_C one observes a plasmino strength, which decreases faster (compare Fig.4.2b) but which has a steeper dispersion relation for momenta bigger than ≈ 0.2 T. The minimum of the plasmino branch has shifted to smaller momenta as well. The values of the slope for small momenta are presented in Table III, where in both cases we do not see the HTL predicted behavior from Eq.(2.29).

To test how well the HTL approximation describes the data, we employ the ansatz Eq.(3.30), which includes two broad contributions from possible excitations. In case the propagators we consider follow the HTL prediction, we expect the two Breit-Wigner functions, on top of the HTL continuum, to have a very small width and show time-like dispersion relations. For the thermal quark mass, a parameter in the

continuum part, we use those extracted from the two-pole ansatz. Before we present the results, we shortly comment upon this idea. In [16] it was found that for an ansatz with two Gaussian functions the width only reduces to zero if the fits were correlated. As mentioned after Eq.(3.18) we assume uncorrelated data in our procedure. Nevertheless we observe a correlation which is encoded in our propagator. From the normalization of the spectral density Eq.(2.41) we can infere the total spectral strength in Eq.(3.25) must equal $\frac{1}{Z_2^W} \gtrapprox 1$. The same has to be true for the total spectral strength for all other ansätze. We find this to be approximately fulfilled in all our approaches. This implies the fitting routine suggests this correlation, based on the data and, in this sense, is correlated.

The investigation of the ansatz with two Breit-Wigner functions Eq.(3.30) plus the HTL suggested continuum contribution Eq.(2.28) gives two Breit-Wigner functions with relative widths presented in Fig.4.3.

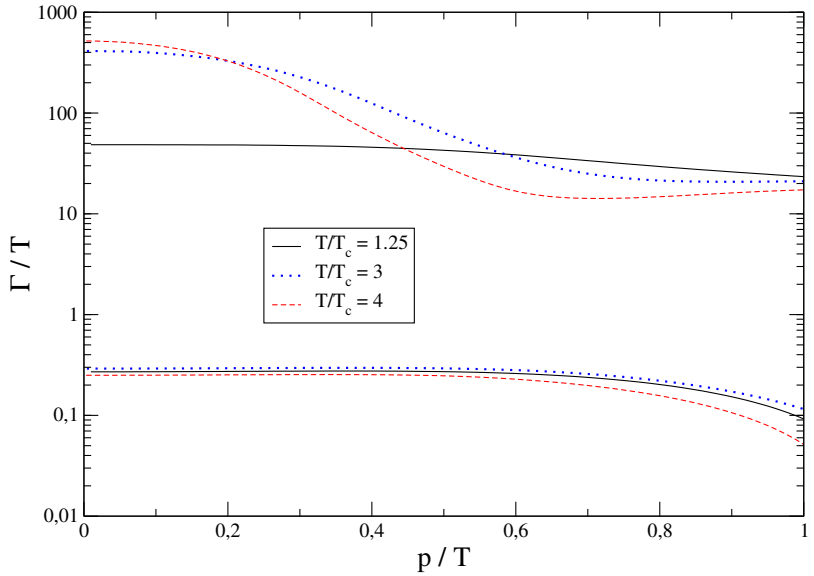

Figure 4.3: Comparison of the obtained width for a Breit-Wigner ansatz Eq.3.30 plus HTL continuum for 1.25 T_C (solid lines), 3 T_C (dotted lines) and 4 T_C (dashed lines)

T/T_C	1.25	4
slope pole 1	0.42	0.26
slope pole 2	(-)0.30	(-)0.14

Table III: Slopes of the dispersion relations in Fig.4.2a.

A remarkable feature is the fact that there is one rather small Breit-Wigner distribution with a width of about 0.2 T for all temperatures, which can be interpreted as a residual of the quark pole. However, the width of the second Breit-Wigner function is very big and tells us immediately that an ansatz with two sharp poles will not describe the spectrum sufficiently, if we use the HTL predicted continuum only. Nevertheless the figure of merit l^2/dof for the ansatz with two Breit-Wigner functions is about two orders of magnitude at T=4 T_C and three orders of magnitude at T=1.25 T_C better compared to the HTL ansatz (see Fig.4.8a). The fact that the relative width of the wide Breit-Wigner function for both higher temperatures in Fig.4.3 is about a factor of ten bigger than the one for 1.25 T_C, might be an indicator that our model for d_1 in Eq.(3.14) overestimates the vertex strength, already indicated by recent lattice values for the thermal mass, as mentioned before. We observe that this width seems to tend to a common limit. In Fig.4.4 the dispersion relations are presented. We see that the rather small Breit-Wigner function has its maximum slightly below the lightcone.

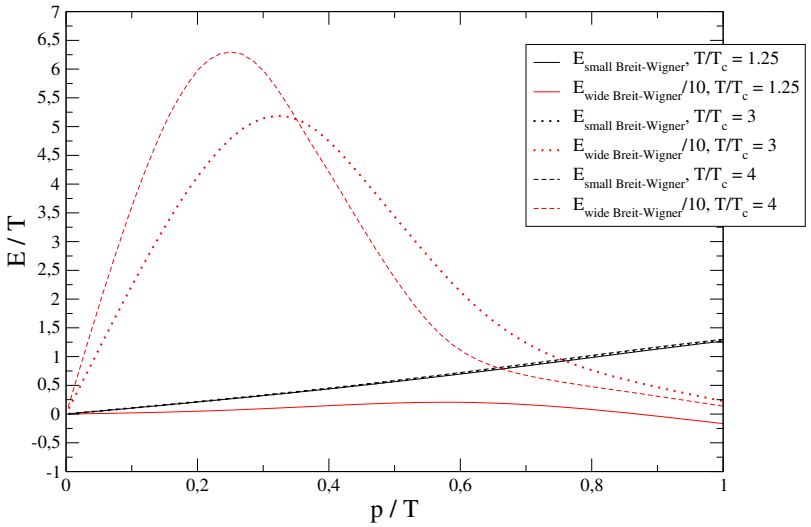

Figure 4.4: Comparison of the obtained dispersion relations for a Breit-Wigner ansatz Eq.(3.30) plus HTL continuum for 1.25 T_C (solid lines), 3 T_C (dotted lines) and 4 T_C (dashed lines)

In [27] it was investigated what impact the shape of the gluon-propagator and the vertex strength might have on the shape of the HTL suggested two-pole structure. The authors employ a Dyson-Schwinger calculation in rainbow-ladder approximation to show that the peak of the fermion spectral function is broadened by in-medium effects for the gauge boson. This might give an explanation why the HTL prediction leaves space for an improved description. Motivated by the findings in [27] we investigate the spectral function for the chirally symmetric phase in the following

with ansatz Eq.(3.31), expecting the additional Breit-Wigner function to mimic the continuum contributions from the gluon-propagator and the influence of the vertex strength. As mentioned before, this was subject to investigation of different minima in l^2. The minima leading to the smallest l^2 we found and the resulting parameters will be presented in the following.

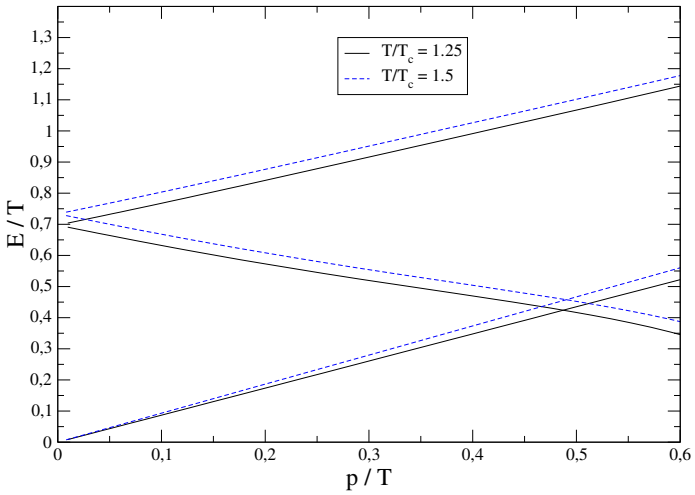

Figure 4.5: Dispersion relation for the HTL with continuum plus Breit-Wigner ansatz for 1.25 T_C (solid lines) and 1.5 T_C (dashed lines).

T/T_C	1.25	1.5	3	4	5
m_T/T	0.6974	0.7335	0.7556	0.7049	0.6671

Table IV: Values for the obtained thermal masses for the HTL plus Breit-Wigner ansatz Eq.(3.31)

In Tabel IV the quark thermal masses for all investigated temperatures are summarized. For 1.5 and 3 T_C they are in good agreement with those recently published in [17]. In Figures 4.5 and 4.6 one can see that the character of the plasmino branch is different for small and high temperatures. While for high temperatures the (anti)particle-like behavior changes, leading to a minimum in the dispersion relation, it stays antiparticle-like for small temperatures. In Table V the slopes of the dispersion relations are summarized and we see, by comparing with Eq.(2.29) and Table III, the slopes for higher temperatures are closer to the HTL prediction than for the HTL ansatz. In Figures 4.5 and 4.6 we observe, the Breit-Wigner function simulates a space-like contribution, which reaches also in the time like region due to the width of the Breit-Wigner function. The mean value is always below the lightcone and raises with a slope smaller than one. It is striking that the behavior is similar

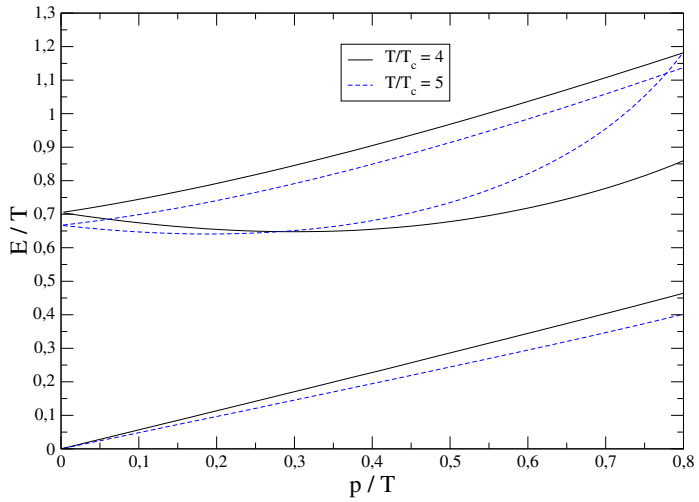

Figure 4.6: Dispersion relation for the HTL with continuum plus Breit-Wigner ansatz for 4 T_C (solid lines) and 5 T_C (dashed lines).

for both small temperatures and for both high temperatures. This reminds of the broadening of the spectral function found in [27]. In Fig.4.7a we see that the Breit-Wigner function contributes with a constant spectral strength, while the antiparticle contribution is damped. This damping seems to differ for the smaller and the higher temperatures, where the smaller temperatures seem to have a smaller damping rate for the plasmino-like contribution. We observe the spectral contribution from the Breit-Wigner function to decrease with increasing temperature, indicating we get closer to the simple HTL continuum description. In Fig.4.7b we see, the width of the continuum slightly increases with the temperature, which might be caused by a slightly overestimated vertex strength parameter. We want to mention that the ansatz works quite well up to momenta of 0.6 T for the small temperatures and up to 0.8 T for the higher temperatures before becoming numerically instable. However, this does not effect its predictive character since the HTL ansatz becomes instable at about $p \approx T$, too.

To finally rate how good a fit is, one has to consider the figure of merit. Looking at Fig.4.8a shows, the description with our chosen ansatz Eq.(3.31) is better than

T/T_C	1.25	1.5	4	5
slope pole 1	0.75	0.74	0.44	0.31
slope pole 2	(-)0.60	(-)0.59	(-)0.24	(-)0.21
slope Breit-Wigner	0.87	0.93	0.57	0.48

Table V: Values for the parameters extracted from Figs.4.5 and 4.6

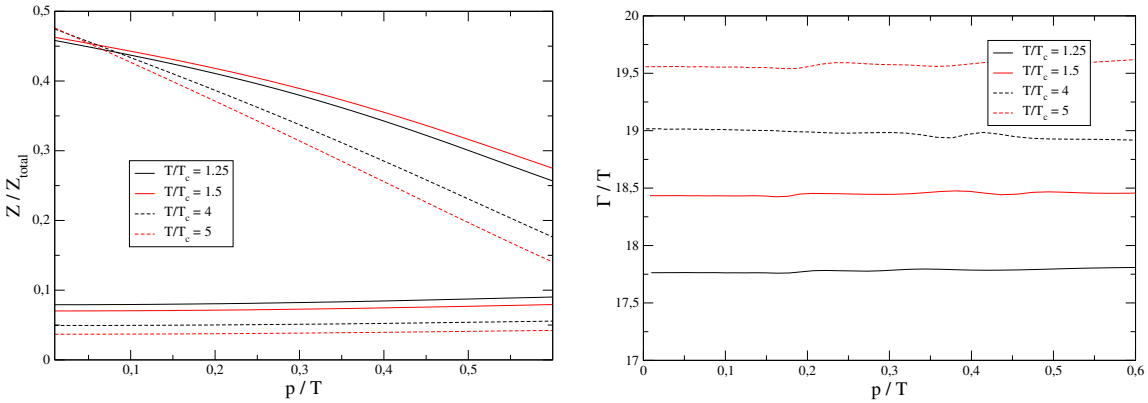

(a) Relative spectral strength

(b) Relative width

Figure 4.7: Relative spectral strength of the plasmino and the almost constant contribution from the Breit-Wigner continuum and relative width of the Breit-Wigner continuum for small (solid lines) and higher (dashed lines) temperatures.

both, the HTL ansatz and the ansatz with two Breit-Wigner functions plus the HTL continuum. This indicates that the picture of the plasmino as an collective phenomena might arise from an antiparticle-like excitation at smaller temperatures as indicated in Fig.4.5. If we look at Fig.4.8b showing the total spectral strength for the different ansätze, we see that the HTL ansatz plus the Breit-Wigner function gives a pretty good and constant value for the total spectral strength related to the wave function renormalization constant by $Z_{total} = 1/Z_2^W \gtrsim 1$. The non-constant character of the ansatz with two Breit-Wigner plus the HTL continuum indicates possible numerical instabilities for this ansatz.
In both Figures, 4.8a and 4.8b, we make the observation that the ansatz works better for higher temperatures.

4.2 Impact of a finite quark mass

In this section we present calculations with our model Eq.(3.14) for quarks with finite bare mass with both, the HTL and the improved HTL ansatz, including the additional Breit-Wigner function. The actual renormalized mass of a quark is non-zero, leading to explicit breaking of chiral symmetry. Therefore it is interesting to investigate the influence of a finite mass on our results for the quark spectral function. In Fig.4.9 we can see the results for the fit with the two-pole ansatz at $|\mathbf{p}| = 0$ for the projection of the scalar function as defined in Eq.(2.38). This is commonly termed thermal mass, a quantity sensitive to the interactions the in-medium particle undergoes. By looking at the plasmino contribution to the spectral function, encoded

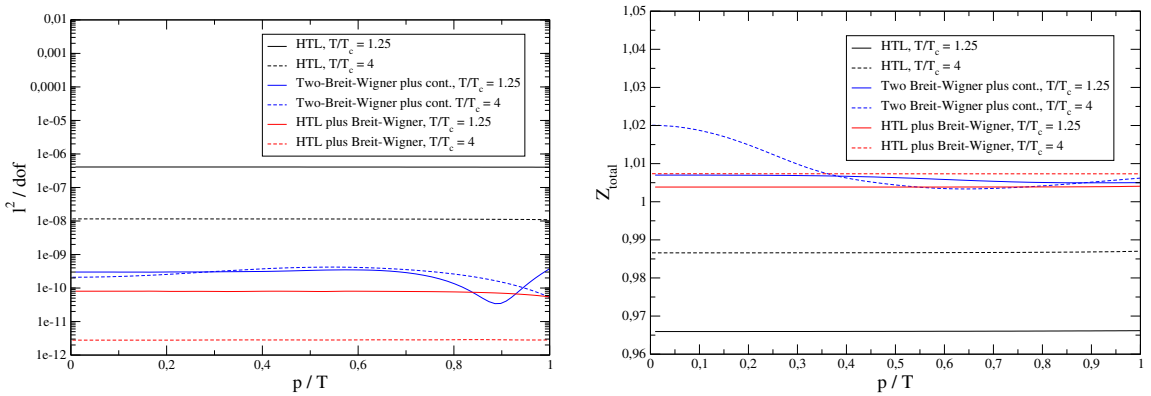

(a) Figure of merit l^2

(b) Total spectral strength

Figure 4.8: Comparison of the values of the figure of merit l^2 for the used ansätze for 1.25 T_C (solid lines) and 4 T_C (dashed lines) in the left panel and of the total spectral strength for the two Breit-Wigner plus continuum Eq.(3.30), the HTL plus Breit-Wigner Eq.(3.31) and the HTL suggested ansatz Eq.(3.23) in the right panel.

in the spectral strength (shown in Fig.4.9b), we see that the influence of the plasmino drops dramatically with increasing bare mass. This behavior was already expected from investigations with heavy quarks, where the spectral function basically reduces to a free quark spectral function.

On the other hand we see a minimum for the thermal mass of the quark at a bare mass of 0.1 T for all temperatures, while the energy for the plasmino increases almost monotonically. This is in accordance with [16], while in comparison with our spectral strength in Fig.4.9b drops faster compared to their results.

For a finite quark mass the projection of the spectral function in Eq.(2.46) is not defined. This is a drawback, since it would be interesting to see the momentum dependence of the spectral strength and the dispersion relations for physical quark mass.

Finally we want to check the results for a finite mass with our improved ansatz. In Fig.4.10 we see about the same behavior of the two poles for the thermal masses while the spectral strength of the plasmino mode drops more dramatically, shown in Fig.4.10b. For completeness we show also the parameters of the Breit-Wigner function in Fig.4.11 which apparently produces a sort of background modulation, due to its broad width and almost linear increase in energy. The second ansatz improves the figure of merit in this context about three to four orders of magnitude in comparison with the HTL ansatz.

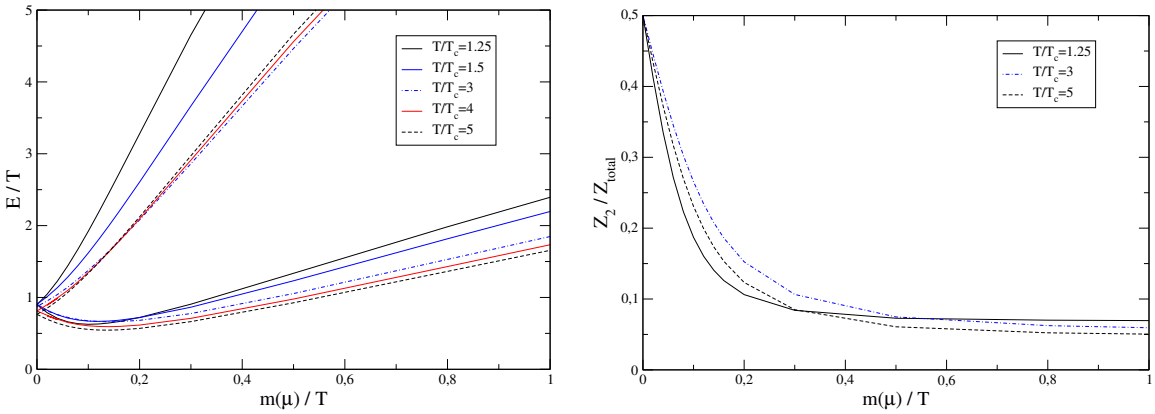

(a) Thermal masses ($|\mathbf{p}| = 0$) (b) Relative strength of the plasmino pole

Figure 4.9: Results for the parameters of the two-pole ansatz in quenched QCD for finite current quark mass at 1.25, 3 and 5 T_C. For the plots we defined $E_2 > E_1$ with E_2 being the plasmino mode energy.

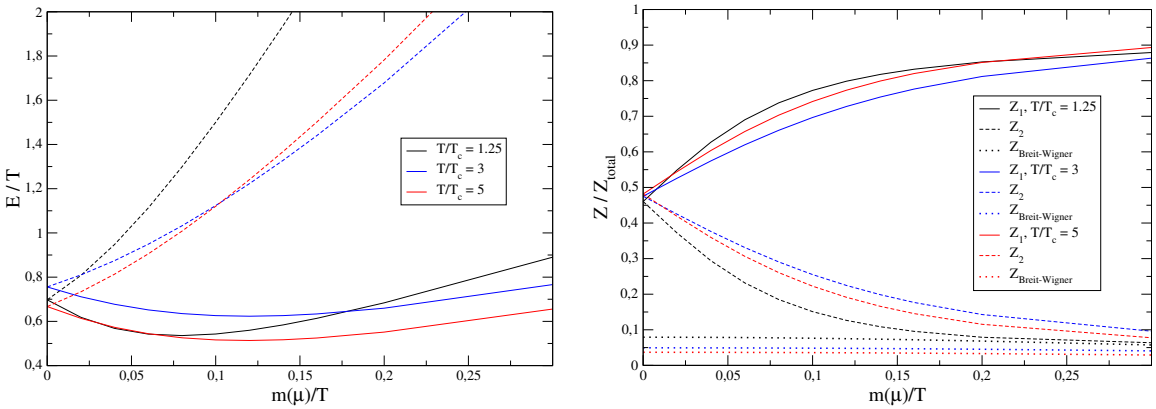

(a) Thermal masses ($|\mathbf{p}| = 0$) (b) Relative strength of the plasmino pole

Figure 4.10: Results for the parameters of the two-pole ansatz plus Breit-Wigner in quenched QCD for finite current quark mass at 1.25 (black lines), 3 (blue lines) and 5 T_C (red lines). For the plots we defined $E_2 > E_1$ with E_2 being the plasmino mode energy.

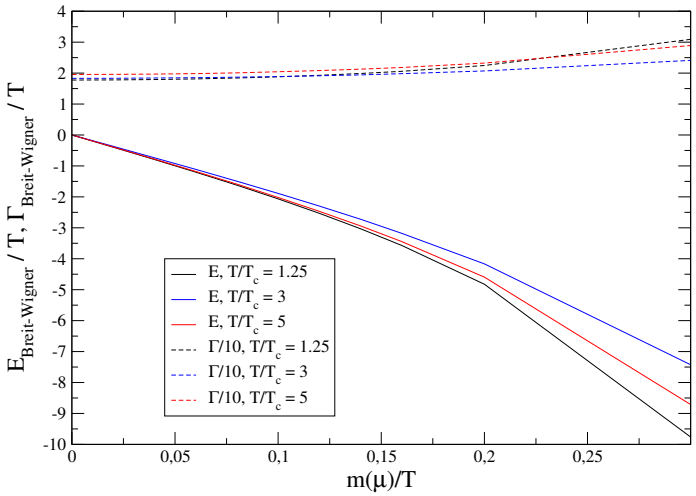

Figure 4.11: Results for the parameters of the Breit-Wigner function for the two-pole ansatz plus Breit-Wigner in quenched QCD for finite current quark mass at 1.25 (black lines), 3 (blue lines) and 5 T_C (red lines).

5 Quark spectral functions in $N_f = 2 + 1$ unquenched QCD

In this last chapter we focus on the scenario of unquenched QCD with $N_f = 2 + 1$ quark flavors. This is the first investigation on the behavior of the quark spectral function in the framework of Dyson-Schwinger equations under our truncation. It is interesting to see whether the behavior predicted by HTL applies, as seen in the previous chapter for the case of quenched QCD. We first draw our attention to the chiral limit for the light quarks and finally to the case of physical quark masses. In both cases we employ ansätze for spectral function without the HTL continuum and use a strange quark mass of $m_s = 54$ MeV.

5.1 Quark spectrum in the chiral limit

An investigation of the chiral limit for unquenched QCD is an useful starting point towards finding an ansatz for the case of physical quark masses. In Ref. [28], a model ansatz for the vertex to calculate quark propagators has been used together with the gap equation and the Maximum Entropy Method. The authors found for the chiral limit not only the common two pole structure in the quark spectral function, but also a third pole which appears as a zero mode and has support only close to the critical temperature. As already discussed, in the chiral limit for unquenched QCD we expect to see a second order phase transition. A striking feature of the results in Ref. [28] is the disappearance of this zero-mode at about 1.35 to 1.8 times the critical temperature.

Estimation of the critical temperature

Before we start investigating the results with the tripole ansatz Eq.(3.27), we want to make an estimation of the critical temperature $T^{2nd}_{unq,chiral}$ for our scheme. In Fig.5.1 one can see the B-function of the propagator is finite for values up to T=136 MeV and then it is, above the critical temperature, zero. Since the mass-function for the DSE propagators is defined as $M(p^2) = B(p^2)/A(p^2)$ and the A-function stays finite, we see the generated mass vanishes at this temperature. In the chiral limit, where

the bare mass vanishes, this is equivalent to chiral symmetry restoration, therefore the critical temperature in this case is $T^{2nd}_{unq,chiral} \approx 137MeV$.

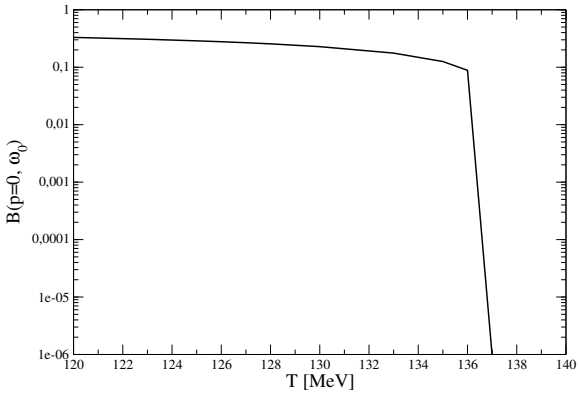

Figure 5.1: B-function at $|\mathbf{p}| = 0$ for the first Matsubara depending on the temperature for unquenched QCD in the chiral limit.

Tripole-ansatz

In order to investigate whether the tripole ansatz fits our propagators we use the two different ansätze for the vertex strength d_1, as defined in Eqs.(3.17) and (3.16). Firstly we test whether the zero-mode on top of the well know two-pole-solution is present in the projections of our spectral functions, defined in Eqs.(2.46) and (2.38), as predicted in Ref. [28].
Fig.5.2a shows the thermal masses for both vertices. One can see that the difference for the quark and plasmino thermal masses between the two vertices increases with the temperature mirroring the different strength d_1(T). In both cases we find a zero-mode for all temperatures we investigated.
In Fig.5.2b we see the spectral strength of the three poles. In contradiction to [28], we see neither for the constant, nor for the model vertex strength, that the zero-mode dies out in the temperature interval we consider (1 to 1.8 $T^{2nd}_{unq,chiral}$). We actually see that the spectral strength of the third pole dominates the two particle-like poles and, by comparing the two ansätze for d_1, whether it has increasing spectral strength or is damped depends on the vertex strength. This might result from the unquenching process and its backcoupling to the quark sector.
The question is, what causes the difference and one possible explanation is the way the spectral functions haven been obtained. The calculations in Ref. [28] are not one to one comparable to our unquenched calculations and so is the ansatz for their vertex. While they used the Maximum Entropy method relying on statistical guidance towards the solution hidden in their quark propagator, we employ a fit ansatz. The interpretation of the zero-mode as the in-medium realization of the Wigner-mode

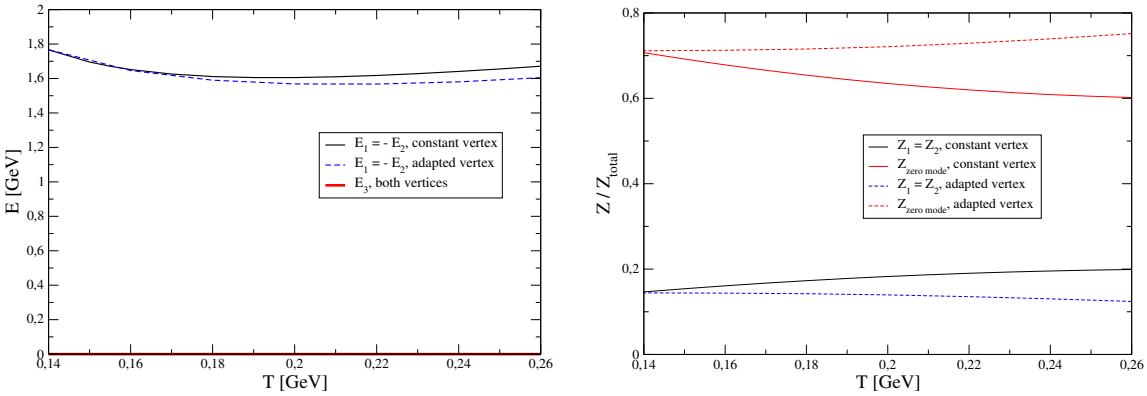

(a) Thermal masses (b) Spectral strengths

Figure 5.2: Thermal masses and spectral strengths for the tripole ansatz for unquenched propagators in the chiral limit with the constant vertex Eq.(3.17) (solid lines) and the vertex model Eq.(3.16) (dashed lines) depending on the temperature.

of our DSEs has to be considered with care. Especially if we look at Fig.5.3a, and compare it to the quenched scenario shown in Fig.4.6, we might interprete this zero-mode rather as a background contribution.
Next we want to consider the dependence of the fit parameters on the momentum for a certain temperature, which was chosen as T=200 MeV. The dispersion relations in Fig.5.3a show an HTL-like behavior for the quark- and plasmino-like poles, while the zero-mode rises linearly and crosses the $E = p$ line.
In Fig.5.3b we see the dependence of the spectral contribution, depending on the momentum, at this temperature. If we interpret the second pole again as the common plasmino we observe the known damping of its spectral contribution in Fig.5.3b. We once again see the spectral domination of the zero-mode pole, which displays an almost constant strength for both ansätze of the parameter d_1.

Ansatz with three Breit-Wigner functions

After we investigated the suggested tripole solution and found the appearance of a third pole, we want to investigate whether there is more involved than three sharp peaks. It turns out that an ansatz, including a width for all three poles and therefore using three Breit-Wigner functions, gives the best description of our data. We use both the constant as well as the model vertex strength to examine this ansatz. In Fig.5.4 we can see what is the influence the vertex strength model makes upon the fit results depending on the temperature. As we see in Fig.5.4a, a pole-like zero-mode for both vertex models exists. At $T \approx 210$ MeV the results for the model vertex seem to merge to a solution, where only the zero-mode is present. The branches, which

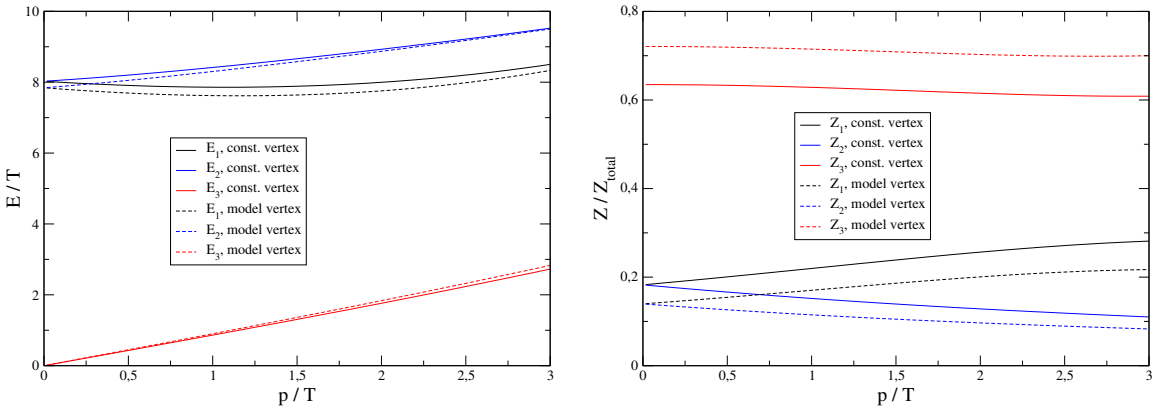

(a) Dispersion relations

(b) Spectral strengths

Figure 5.3: Dispersion relations and spectral strengths for the tripole ansatz for unquenched propagators in the chiral limit with the constant vertex Eq.(3.17) (solid lines) and the vertex model Eq.(3.16) (dashed lines) at a temperature of 200 MeV.

appear at this temperatures in the width and the spectral contribution, are redundant, since they basically merge to one common value for this zero-mode. For the constant vertex, the width of the zero-mode increases slightly with the temperature, while the quark- and plasmino like Breit-Wigner functions, with the same absolute value for the energy, have the same (almost constant) width and a slightly decreasing thermal mass.
If we draw our attention to the spectral strengths in Fig.5.5, we find the same behavior as in the case of the tripole ansatz. The zero-mode dominates the spectrum and whether its damped or it rises depends on the vertex strength. The decreasing vertex strength from the model Eq.(3.17) for the vertex parameter d_1 leads to a decreasing contribution, while the constant vertex results in a slight increase. The last case with fixed d_1 leads to the same spectral strength for the plasmino- and quark-like Breit-Wigner function with a slight damping, while in the model for the vertex the spectral contribution for the quark-like and the plasmino-like branch differ in their dependence on the temperature.

Next we want to examine the behavior for the three Breit-Wigner functions depending on the momentum for a certain temperature. We want to compare the results to those for the tripole ansatz and therefore we choose again a temperature of 200 MeV. In Fig.5.6 we see the dispersion relations and the relative widths of the Breit-Wigner functions for this case. It is apparent that the impact of the vertex strength is more important compared to the tripole ansatz (compare Fig.5.3). For the first Breit-Wigner function (we identify as quark-like), the observation is that this branch seems to approach free particle behavior for large momenta. The second Breit-Wigner function (plasmino-like), displays the known pattern of a minimum

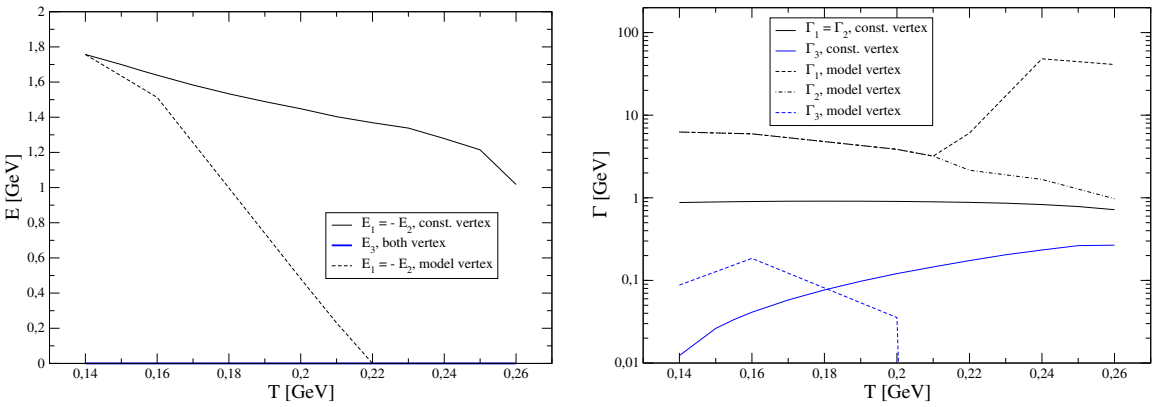

(a) Thermal masses (b) Widths

Figure 5.4: Thermal masses and widths of the Breit-Wigner functions for unquenched propagators in the chiral limit with the constant vertex Eq.(3.17) (solid lines) and the vertex model Eq.(3.16) (dashed lines) at $|\mathbf{p}| = 0$ depending on the temperature.

in the dispersion relation, just as in the quenched case. This minimum is followed by almost free particle behavior, with a different group velocity then the quark-like pole. The position of the minimum strongly dependents on the vertex strength, in contradiction to the tripole ansatz. For the constant vertex strength, the long range, almost linear behavior for the quark and the plasmino branch, in form of one particle-like and an one antiparticle-like dispersion relation, reminds of the quenched case in Fig.4.5 for small temperatures. The slopes are 1.23, respectively -1.48, and therefore much larger than in the quenched scenario.
The widths of the quark- and plasmino-like Breit-Wigner functions in Fig.5.6b show similar behavior for constant d_1. However, when we apply the model vertex, they mirror the shape of the dispersion relations. An interesting phenomena appears for the third Breit-Wigner function representing the zero-mode. For the constant vertex strength the relative width decreases monotonically towards a pole-like behavior at large momenta, while for the model vertex strength, set up in Eq.(3.16), we find an increase from an essentially zero width reaching a maximum at about 0.2 T for $p \approx 2$ T before it tends to zero again.
The spectral strength at T=200 MeV, shown in Fig.5.7, reveals for small momenta the same behavior as with the tripole ansatz (damping of the plasmino like and rising of the quark like contribution) but then shows an increase of the zero-mode for higher momenta and simultaneous damping of both, the quark- and plasmino-like contribution. This happens for the model vertex earlier as for the constant vertex strength. For the model vertex all three contributions tend to a constant value.

An evaluation of this results at T=200 MeV can be done by looking at Fig.5.8. We see that the figure of merit for the three Breit-Wigner function ansatz is better

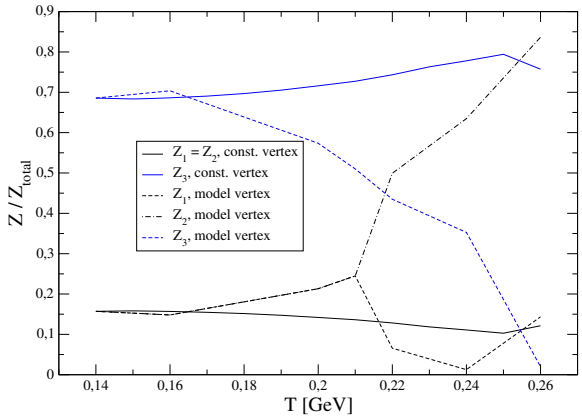

Figure 5.5: Spectral strengths for the three Breit-Wigner ansatz for unquenched propagators in the chiral limit with the constant vertex Eq.(3.17) (solid lines) and the vertex model Eq.(3.16) (dashed lines) depending on the temperature.

than for the tripole ansatz and Z_{total} is closer to the expected value of $1/Z_2^W$.

Since the shape of the dispersion relations for both ansätze reminds of the HTL pattern, we want to make some connections trying to match the effects of the unquenching process. In chapter 4 we found an ansatz with two poles, the HTL-continuum and an additional Breit-Wigner function to model the in-medium effects of the gluon-propagator. The tripole and the ansatz with three Breit-Wigner functions displays the appearance of a third excitation in the space-like region. While the pole character of this contribution to the spectrum was given with the tripole ansatz, the three Breit-Wigner ansatz shows we rather face an excitation with a certain width which is also true for the two poles. The contribution we call zero-mode might be a combination of Landau damping, the in-medium contribution of the gluon and unquenching effects, which additionally might cause the finite width of the poles we found in the quenched case.

The Schwinger function in the chiral limit

Finally we want to investigate the Schwinger function, calculated with Eq.(2.49), for a constant vertex strength parameter. Firstly, we used the tripole ansatz to calculate the propagator, also for temperatures below the critical temperature. This leads to a l^2 of about three orders of magnitude smaller compared to the figure of merit for the ansatz above the critical temperature. In Fig.5.9a we ploted the Schwinger functions for four different temperatures. One notices two important features reflected in this results:

- We observe the reflection of the chiral restoration as shown in Eq.(2.51) for temperatures above $T^{2nd}_{unq,chiral}$.

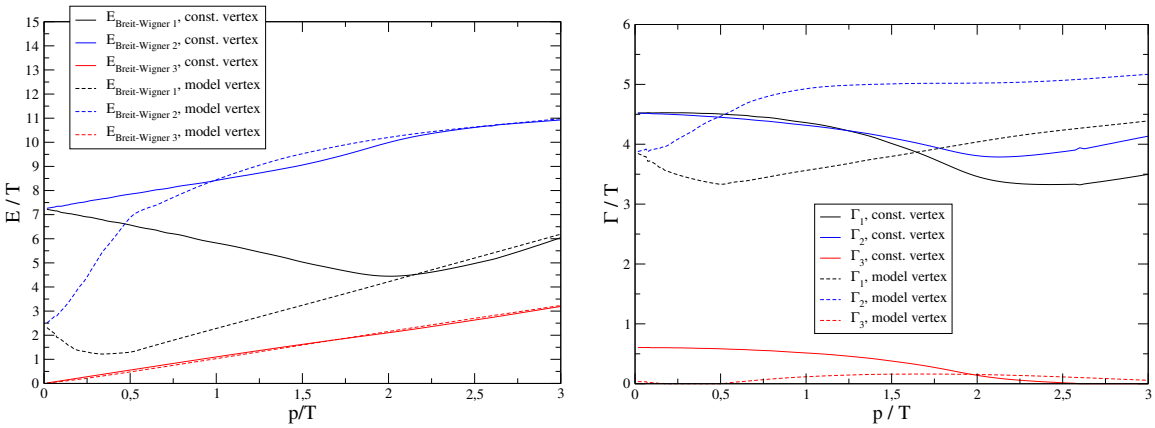

(a) Dispersion relations

(b) Relative widths

Figure 5.6: Dispersion relations and relative widths for the three Breit-Wigner ansatz for unquenched propagators in the chiral limit with the constant vertex Eq.(3.17) (solid lines) and the vertex model Eq.(3.16) (dashed lines) at a temperature of 200 MeV.

- We do not observe a concave curvature below $T^{2nd}_{unq,chiral}$ nor is the Schwinger-function negative in the regime down to 110 MeV.

Since we consider the chiral limit, the first point was expected, while the second comes unexpected. Since we did not exclude negative solutions for our spectral function, this could be related to the limitations of our ansatz. They might lead to the solution of the Schwinger function which has no convex curvature. Exploring the ansatz with three Breit-Wigner functions, we find a better description below the critical temperature (compare Fig.5.10). The Schwinger functions are given in Fig.5.9b and show the expected concave curvature, implying positivity violations. This shows the importance of the actual fit to the data below T_C and the sensitivity of the Schwingerfunction. From the results for the Schwinger function obtained with the ansatz including three Breit-Wigner functions we derive, that the deconfinement and the chiral phase transition happen at about the same temperature.

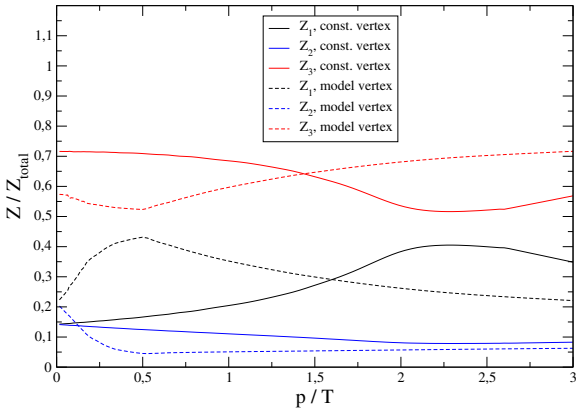

Figure 5.7: Spectral strengths for the three Breit-Wigner ansatz for unquenched propagators in the chiral limit with the constant vertex Eq.(3.17) (solid lines) and the vertex model Eq.(3.16) (dashed lines) at a temperature of 200 MeV.

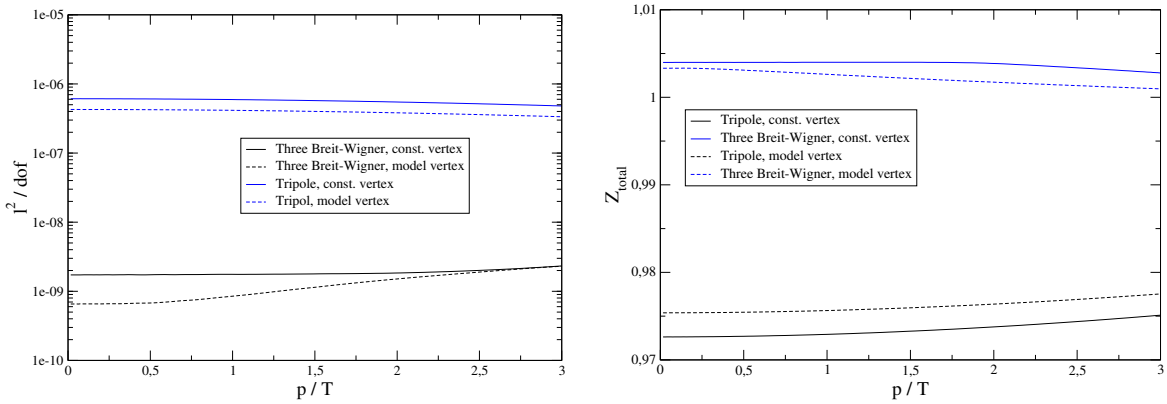

(a) Figure of merit $l^2(p)$

(b) Total spectral strength $Z_{total}(p)$

Figure 5.8: Comparison of the figure of merit $l^2(p)$ and the total spectral strengths for the three Breit-Wigner functions and the tripole ansatz for unquenched propagators in the chiral limit with the constant vertex Eq.(3.17) (solid lines) and the vertex model 3.16 (dashed lines) at a temperature of 200 MeV.

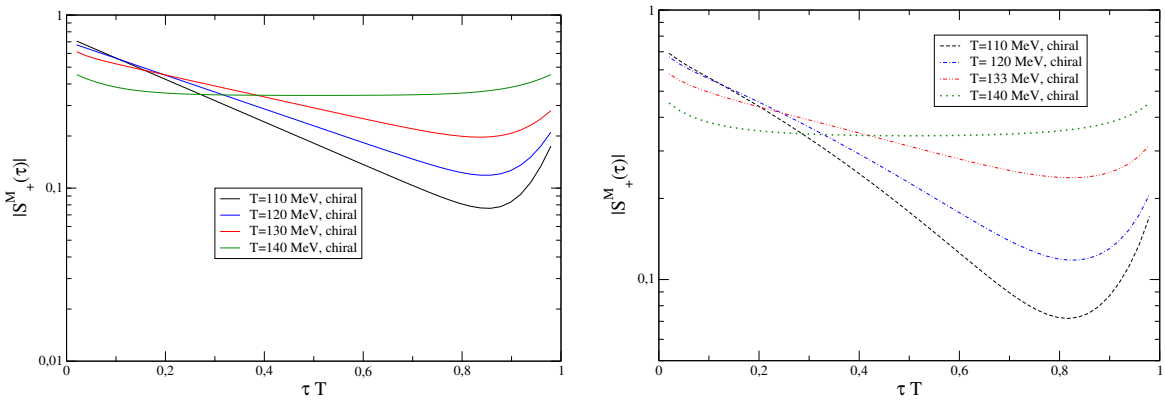

(a) Tripole ansatz (b) Three Breit-Wigner ansatz

Figure 5.9: Schwinger functions for the tripole ansatz and the ansatz with three Breit-Wigner functions for unquenched propagators in the chiral limit with the constant vertex Eq.(3.17) at different temperatures below and above $T^{2nd}_{unq,chiral}$.

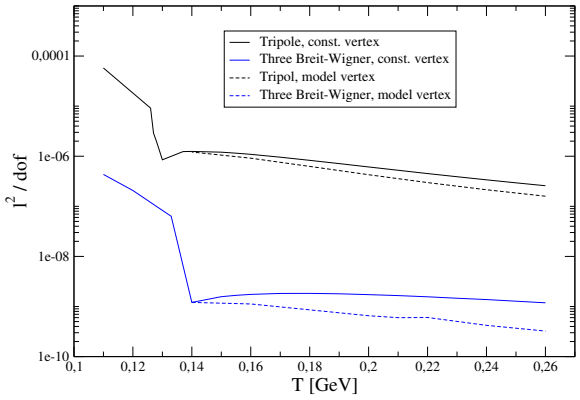

Figure 5.10: Figure of merit $l^2(T)$ for the unquenched propagators in the chiral limit with the constant vertex Eq.(3.17) at different temperatures below and above $T^{2nd}_{unq,chiral}$.

The quark spectral function for T=200 MeV in the chiral limit

Finally, we want to investigate the three-dimensional appearance of the quark spectral function in the chiral limit. We choose again a temperature of 200 MeV, the ansatz with three Breit-Wigner functions and employed the vertex model Eq.(3.16). In Fig.5.11 we see the dependence of the resulting spectral function on the energy ω and the absolute value of the three-momentum $|\mathbf{p}|$. We observe that only the zero-mode appears, which was already indicated in Figures 5.6 and 5.7. The increase of the zero-mode in the spectral function is related to the increasing spectral strength, shown in Fig.5.7. The behavior for small momenta (energies), where a minimum is displayed, seems to be related to the partly finite width and decreasing strength of the zero-mode and the influence of the quark-like branch.

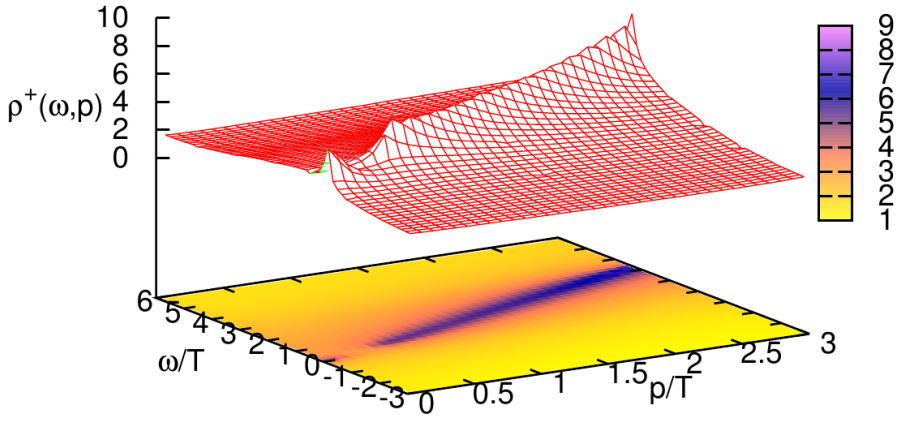

Figure 5.11: The quark spectral function calculated with the vertex model Eq.(3.16) at a temperature of 200 MeV.

5.2 Spectrum for physical quark masses

The last section is dedicated to a calculation with physical up- and down quark masses of 2 MeV. In this setup the projection of the spectral function as in Eq.(2.46) is not applicable, since we are not in the chiral limit. Nevertheless, we can investigate the infrared behavior of our spectral functions at $|\mathbf{p}| = 0$ and test which ansatz works at this point. It is also possible to investigate the Schwinger function for finite masses. As mentioned before we apply a constant vertex strength as well as the adapted vertex strength fitted to the chiral condensate results of lattice QCD (see Eq.(3.15)). In this setup we do not expect a critical temperature but a crossover

at about $T^{cross}_{unq,phys} \approx 156$ MeV. To illustrate this, we once again consider the scalar dressing function at zero momentum for the first Matsubara mode, which is shown in Fig.5.12. We observe no sharp but a slow decrease in the B-function for the first Matsubara mode at $|\mathbf{p}| = 0$, which signals the crossover character of the phase transition.

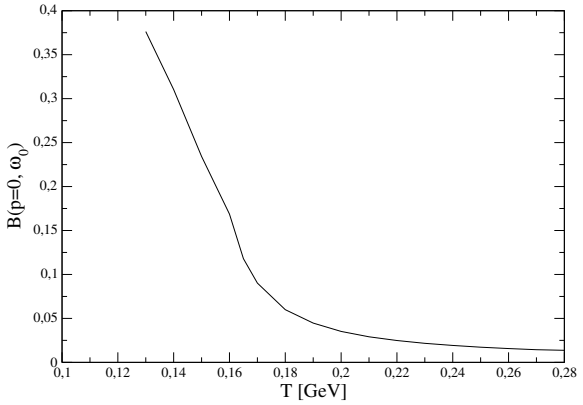

Figure 5.12: B-function at $|\mathbf{p}| = 0$ for the first Matsubara depending on the temperature for unquenched QCD for a bare mass of 2 MeV.

Thermal masses and spectral strength for $|\mathbf{p}| = 0$

Motivated by the results obtained in the chiral limit, one might expect the ansatz with three Breit-Wigner functions to be a good starting point for investigations at very small quark masses compared to the temperature scale. Nevertheless, we want to start by considering a tripole ansatz before turning to the three Breit-Wigner functions. In Fig.5.13 we compare the thermal masses for the constant and the model vertex strength parameter. Far away from the crossover, at about T=220 MeV, the ansatz tends towards the solution we encountered in the chiral limit, with two poles of the same energy (but different signs) and one zero-mode. The same behavior is also reflected in the relative spectral strength (see Fig.5.15a). The observations are true for both vertices, with the difference that the reduced vertex strength of the adapted vertex seems to be reflected in the stronger decrease of the zero-mode like pole as shown in Fig.5.15b. It is also striking that the thermal mass appears to be temperature independent above about 200 MeV for both vertices.

An interesting feature is also the behavior below 140 MeV. The tripole ansatz suggests a two-pole solution below about 130 MeV and then picks up a third pole appearing at a very high thermal mass. One needs to be careful in extracting information from this results since the figure of merit is rather poor in this regime, as we will see in Fig.5.17b. However, Fig.5.17b also shows the tripole ansatz gives a better description below the crossover than the second ansatz, we found to work best above

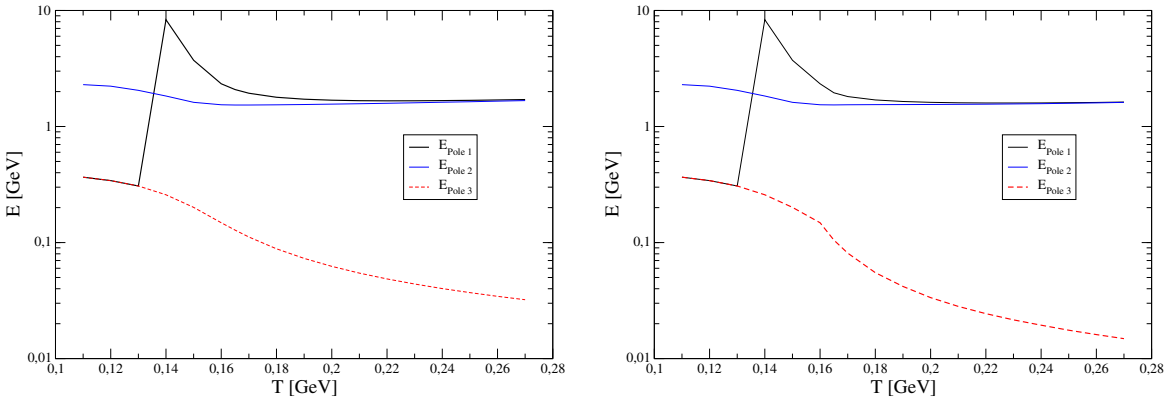

(a) Constant vertex (b) Adapted vertex

Figure 5.13: Thermal masses for the tripole ansatz for unquenched propagators with bare masses of 2 MeV for the two vertex models depending on the temperature.

the crossover temperature.
By starting with three Breit-Wigner functions, we have been guided to an ansatz with one Breit-Wigner function and a pole (compare Eq.(3.32)), which works the best above the crossover temperature. In Fig.5.14 the related thermal masses and the width of the Breit-Wigner function are shown. It seems as one of the poles we observe before the phase transition starts to melt down during the crossover and becomes a sort of underlying background for the pole. The impact of the reduced vertex strength in the adapted vertex is, that the thermal mass of the pole for higher temperatures is pushed down. By looking at the spectral contributions we observe, the Breit-Wigner function overtakes the major contribution to the spectrum from the pole at roughly T=180 MeV. This might be related to the crossover process and the backcoupling the Yang-Mills sector, which is sensitive to the chiral dynamics of the quark sector in our unquenched calculation. If we compare with Fig.5.13 it appears that the Breit-Wigner function can be identified with the role of the zero-mode giving a spacelike contribution to the spectral function. This might be related to Landau damping and other continuum effects, such as the impact of in-medium effects of the gluon propagator discussed in the previous chapter.

In order to evaluate the quality of the fits for the unquenched propagator at physical masses, we look at Fig.5.17b and see that the second ansatz works better than the tripole ansatz above the (pseudo) phase transition. We do also observe that the adapted vertex works better for both ansätze, which is a success of the adaption to the lattice results for the regularized condensate. The increase in the figure of merit for the Breit-Wigner plus pole ansatz at about 260 MeV might be related to the adapted vertex strength. As already mentioned in our discussion of the DSE framework, this model for the vertex strength parameter d_1 is valid only up to the phase

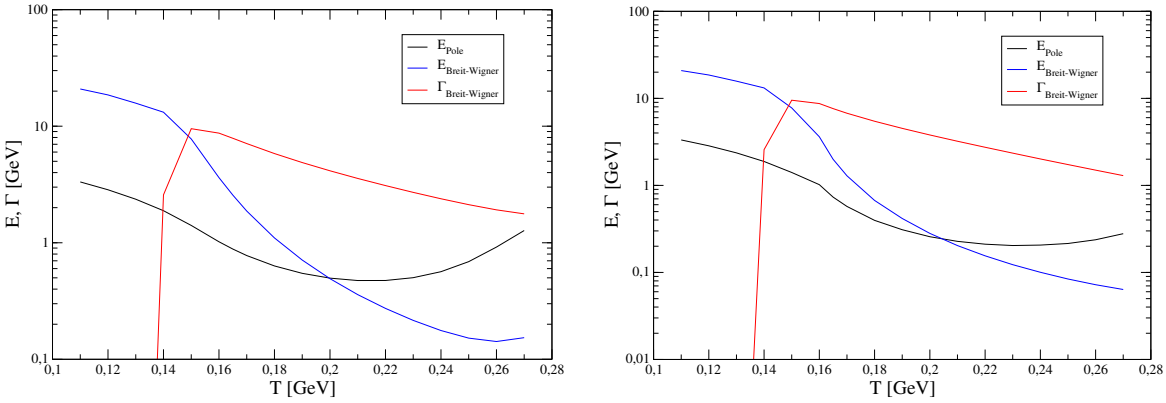

(a) Constant vertex (b) Adapted vertex

Figure 5.14: Thermal masses and widths for the Breit-Wigner plus pole ansatz for unquenched propagators with bare masses of 2 MeV for the two vertex models depending on the temperature.

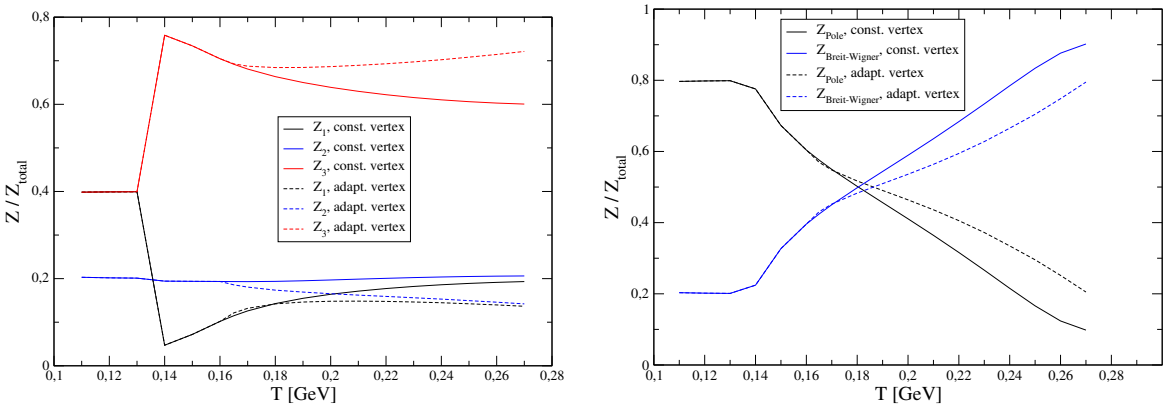

(a) Tripole ansatz (b) Breit-Wigner plus pole ansatz

Figure 5.15: Relative spectral strengths for both ansätze for unquenched propagators with bare masses of 2 MeV for the constant vertex (solid lines) and the adapted vertex (dashed lines) depending on the temperature.

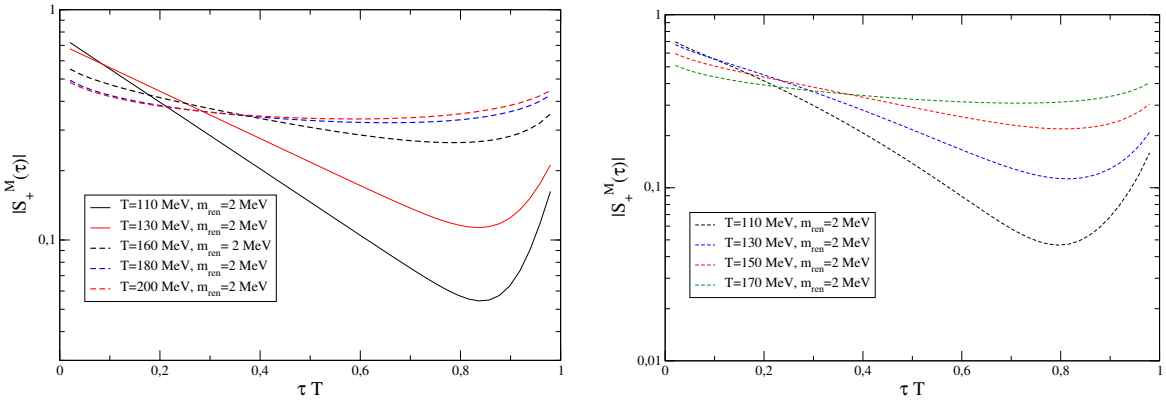

(a) Breit-Wigner plus pole ansatz

(b) Three Breit-Wigner ansatz

Figure 5.16: Schwinger functions for the Breit-Wigner plus pole and the three Breit-Wigner ansatz for unquenched propagators with a bare mass of 2 MeV with the adapted vertex Eq.(3.17) at different temperatures.

transition of the quenched case, where we expect residual effects from the quenched gluon propagator due to the way we invoke the unquenching process.

The Schwinger function for physical masses

Finally, we return to the Schwinger function to inspect possible positivity violations. In Fig.5.16a the calculated Schwinger function from the Breit-Wigner plus pole ansatz is shown. We see that the symmetry from Eq.(2.51) is approached for high temperatures. Due to the finite renormalized quark mass this symmetry will not be achieved exactly, since chiral symmetry is explicitly broken. The same phenomenon in the curvature of the Schwinger function for the investigated temperatures as in the chiral limit is displayed in Fig.5.16a. No change in the sign of the Schwinger function, implying a positive spectral function, without confinement, is possible. This appears unlikely, since in Ref. [32] the temperature for the deconfinement was found to be at about 165 MeV, as shown in Fig.2.6. Therefore we investigated the regime below T=165 MeV, just as in the chiral case, with an ansatz with three Breit-Wigner functions. In Fig.5.16b we can see the resulting Schwinger functions now showing a concave curvature implying the positivity violations we expected. In Fig.5.17b we already saw, that we obtain a better description in terms of a smaller $l^2(T)$ below T=170 MeV with the ansatz with three Breit-Wigner functions, before it reduces to the Breit-Wigner plus pole ansatz, we found to work the best above $T \approx 157$ MeV. This reduction from three Breit-Wigner functions towards one pole and one Breit-Wigner function is displayed in Fig.5.17a. We see that two of the three Breit-Wigner functions collapse to poles, represented in the meltdown of the width, which is driven to essentially zero.

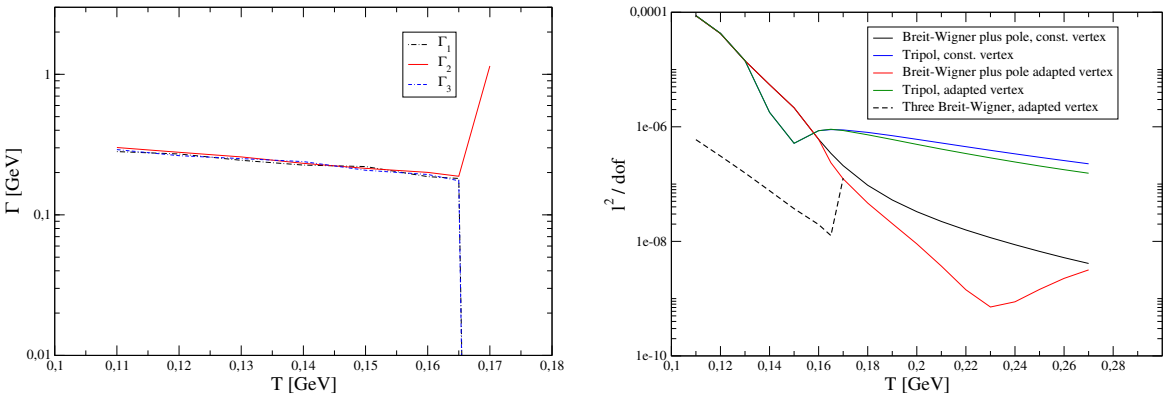

(a) Widths

(b) Figure of merit $l^2(T)$

Figure 5.17: Widths for the three Breit-Wigner functions with the adapted vertex Eq.(3.17) and figure of merit $l^2(T)$ at $|\mathbf{p}| = 0$ for the tripole and the Breit-Wigner plus pole ansatz depending on the temperature for unquenched QCD for a bare mass of 2 MeV .

6 Conclusion and outlook

In this Master thesis the quark spectral function has been investigated for finite temperature quenched and $N_f = 2 + 1$ unquenched QCD at zero quark chemical potential . A Dyson-Schwinger approach has been employed to calculate the quark propagator, which is the main ingredient in the calculation of the quark spectral function. In our truncation scheme, the quark-gluon vertex is based on the first term of the Ball-Chiu vertex, modified with a temperature dependent dressing function. The strength parameter d_1, as a main parameter of this dressing function, was fixed by comparison with lattice results for the thermal mass in the quenched case, and to the chiral condensate for unquenched case with physical masses. Moreover a simple d_1-model for unquenched QCD in the chiral limit was introduced. In the unquenched case, the truncation scheme involved a method to add the quark loop in the gluon DSE, hereby the quenched gluon propagator is calculated with lattice QCD.
Different ansätze for the spectral function, motivated by HTL and previous works, have been presented. Furthermore we introduced the Levenberg-Marquardt algorithm as a method to perform multiparametrical fits, which we have then used to extract the spectral function from the quark propagator.
Firstly we drew our attention to the case of quenched QCD. A comparison with previous results in Ref. [33] proved our algorithm to work. Using the model for the vertex strength parameter d_1, calculations at higher temperatures and with a different ansätze have been carried out. It turned out that the ansatz suggested by HTL, namely two poles and a continuum originating from Landau damping, had to be extended with a Breit-Wigner function. For small temperatures we found two excitations with almost linear dispersion relations, one particle- and one antiparticle-like. For higher temperatures we recovered the HTL picture with a minimum of the so called plasmino pole, the excitations showing antiparticle like behavior for small momenta. The spectral strength of the excitations have been investigated showing a damping of the plasmino. Lastly, we have also investigated the influence of a finite quark mass in the quenched case. The HTL prediction of a plasmino damped at finite masses proved to be true in our extended ansatz.
We then focused on the chiral limit of unquenched QCD using two models for the parameter d_1. For this case Ref. [28] predicts the appearance of a third pole manifested as a zero-mode. We tested this prediction and obtained a solution indicating the existence of this zero-mode. As opposed to the work in [28], the third pole does not disappears in our calculations. Furthermore an ansatz with three Breit-Wigner functions has been employed displaying a finite width for all three poles, one showing

the zero-mode behavior. The width for this zero-mode turned out to be rather small, while the widths of the other poles showed almost constant behavior for a variation of the temperature. The dispersion relations show HTL-like behavior, indicating that the predictions from this high temperature approximation might provide the underlying pattern even for unquenched QCD. We turned to the investigation of the Schwinger function and found a concave curvature below the critical temperature for the second order phase transition, indicating positivity violations and therefore confinement.
The last chapter was dedicated to unquenched QCD with physical quark masses. In this case it was only possible to investigate the behavior for $|\mathbf{p}|=0$. The investigations show the disappearance of the zero-mode, while the spectrum above the crossover at vanishing spatial momentum is described quite well by an ansatz with one pole and one Breit-Wigner function. Finally we revisited the Schwinger function and found positivity violations for a three Breit-Wigner ansatz below the crossover, which merged into the pole plus Breit-Wigner function solution above the (pseudo) critical temperature for the crossover.

To summarize, in this work we have found that the spectral function is extremely sensitive on the running of the vertex strength. Future investigations could focus on a more advanced description of this quantity, eventually derived from further studies on the lattice. This could be obtained by comparing the chiral condensate in the chiral limit, if possible up to high temperatures.
Using the Maximum Entropy method as an alternative to our fitting procedure might also give new insight in the shape of the quark spectral function. Due to time constraints we leave this method for future investigations.
Lastly, in order to reach the final goal of understanding the spectrum of the realistic unquenched QCD for physical masses, it is desirable to develop a method to consider the dispersion relations, specially in the view of making predictions for experiments in order to test the results.

7 Acknowledgment

The support of a lot of people paved the way to finish this thesis and I want to take the opportunity to thank all of them.
First I want to thank my thesis advisor Christian Fischer for giving me the opportunity to work on this fascinating topic and for his guidance and support throughout the last months, whenever needed.
Next I would like to thank professor Wolfgang Cassing for being the second examiner of this work and his interest in its content.
Very important to me was the help by Jan Lücker, who not only shared his knowledge about finite temperature QCD and Dyson-Schwinger equations as well as his program for the calculations of the quark propagator with me, but also proof-read the thesis in the end. I am truely grateful for the help of Jacqueline Bonnet, who did also proof-read my thesis, and especially for the support of Carina Popovici, who introduced me to the details of the APS conventions and checked my thesis concerning terminology. I also want to thank Stefan Strauss for all the fruitful discussions and his persistent interested in my work.
It is with particular pleasure that I thank my friends and family. Especially I would like to mention my mother and sister, whose support and care ensured that I find enough time for my work. Last but not least I want to thank my girlfriend Saskia for her understanding and support as well as for distracting me from my work every now and then.

8 Bibliography

[1] J. Letessier and J. Rafelski, *Hadrons and Quark Gluon Plasma; new ed.* Cambridge monographs on particle physics, nuclear physics, and cosmology, Cambridge: Cambridge Univ., 2005.

[2] J. A. Müller, *A Dyson-Schwinger Approach to Finite Temperature QCD*. PhD thesis, TU Darmstadt, January 2011.

[3] W. Cassing and E. Bratkovskaya, "Parton transport and hadronization from the dynamical quasiparticle point of view," *Phys.Rev.*, vol. C78, p. 034919, 2008.

[4] W. Cassing and E. Bratkovskaya, "Covariant transport approach for strongly interacting partonic systems," *J.Phys.Conf.Ser.*, vol. 230, p. 012001, 2010.

[5] B. Muller and J. L. Nagle, "Results from the relativistic heavy ion collider," *Ann.Rev.Nucl.Part.Sci.*, vol. 56, pp. 93–135, 2006.

[6] E. Shuryak, "Physics of Strongly coupled Quark-Gluon Plasma," *Prog.Part.Nucl.Phys.*, vol. 62, pp. 48–101, 2009.

[7] P. Braun-Munzinger and J. Wambach, "The Phase Diagram of Strongly-Interacting Matter," *Rev.Mod.Phys.*, 2008.

[8] E. Braaten and R. D. Pisarski, "Soft amplitudes in hot gauge theories: A general analysis," *Nuclear Physics B*, vol. 337, no. 3, pp. 569 – 634, 1990.

[9] R. D. Pisarski, "Scattering Amplitudes in Hot Gauge Theories," *Phys.Rev.Lett.*, vol. 63, p. 1129, 1989.

[10] E. Braaten and R. D. Pisarski, "Resummation and gauge invariance of the gluon damping rate in hot qcd," *Phys. Rev. Lett.*, vol. 64, pp. 1338–1341, Mar 1990.

[11] E. Braaten, R. D. Pisarski, and T. C. Yuan, "Production of soft dileptons in the quark-gluon plasma," *Phys. Rev. Lett.*, vol. 64, pp. 2242–2245, May 1990.

[12] J. Casalderrey-Solana, H. Liu, D. Mateos, K. Rajagopal, and U. A. Wiedemann, "Gauge/String Duality, Hot QCD and Heavy Ion Collisions," 2011.

[13] F. Karsch, *Lattice QCD at High Temperature and Density*, vol. 583 of *Lecture Notes in Physics*. Springer Berlin / Heidelberg, 2002.

[14] M. Hamada, H. Kouno, A. Nakamura, T. Saito, and M. Yahiro, "Quark propagators at finite temperature with the clover action," *PoS*, vol. LAT2006, p. 136, 2006.

[15] F. Karsch and M. Kitazawa, "Spectral properties of quarks above in quenched lattice qcd," *Physics Letters B*, vol. 658, no. 1–3, pp. 45 – 49, 2007.

[16] F. Karsch and M. Kitazawa, "Quark propagator at finite temperature and finite momentum in quenched lattice QCD," *Phys.Rev.*, vol. D80, p. 056001, 2009.

[17] O. Kaczmarek, F. Karsch, M. Kitazawa, and W. Soldner, "Thermal mass and dispersion relations of quarks in the deconfined phase of quenched QCD," *Phys.Rev.*, vol. D86, p. 036006, 2012.

[18] Z. Fodor and S. Katz, "Finite temperature and chemical potential in lattice QCD and its critical point," pp. 180–187, 2002.

[19] M. Lombardo, "Lattice QCD at finite density: Imaginary chemical potential," *PoS*, vol. CPOD2006, p. 003, 2006.

[20] M. Kitazawa, T. Kunihiro, and Y. Nemoto, "Quark spectrum above but near critical temperature of chiral transition," *Phys.Lett.*, vol. B633, pp. 269–274, 2006.

[21] P. Maris and C. D. Roberts, "Dyson-Schwinger equations: A Tool for hadron physics," *Int.J.Mod.Phys.*, vol. E12, pp. 297–365, 2003.

[22] R. Alkofer and L. von Smekal, "The Infrared behavior of QCD Green's functions: Confinement dynamical symmetry breaking, and hadrons as relativistic bound states," *Phys.Rept.*, vol. 353, p. 281, 2001.

[23] C. S. Fischer, "Infrared properties of QCD from Dyson-Schwinger equations," *J.Phys.*, vol. G32, pp. R253–R291, 2006.

[24] C. S. Fischer, A. Maas, and J. M. Pawlowski, "On the infrared behavior of Landau gauge Yang-Mills theory," *Annals Phys.*, vol. 324, pp. 2408–2437, 2009.

[25] C. D. Roberts and S. M. Schmidt, "Dyson-Schwinger equations: Density, temperature and continuum strong QCD," *Prog.Part.Nucl.Phys.*, vol. 45, pp. S1–S103, 2000.

[26] M. Blank and A. Krassnigg, "The QCD chiral transition temperature in a Dyson-Schwinger-equation context," *Phys.Rev.*, vol. D82, p. 034006, 2010.

[27] M. Harada and S. Yoshimoto, "Disappearance of quasi-fermions in the strongly coupled plasma from the Schwinger-Dyson equation with in-medium gauge boson propagator," 2009.

[28] S.-x. Qin, L. Chang, Y.-x. Liu, and C. D. Roberts, "Quark spectral density and a strongly-coupled QGP," *Phys.Rev.*, vol. D84, p. 014017, 2011.

[29] C. S. Fischer and J. A. Mueller, "Chiral and deconfinement transition from Dyson-Schwinger equations," *Phys.Rev.*, vol. D80, p. 074029, 2009.

[30] C. S. Fischer, J. Luecker, and J. A. Mueller, "Chiral and deconfinement phase transitions of two-flavour QCD at finite temperature and chemical potential," *Phys.Lett.*, vol. B702, pp. 438–441, 2011.

[31] J. Lucker and C. S. Fischer, "Two-flavor QCD at finite temperature and chemical potential in a functional approach," *Prog.Part.Nucl.Phys.*, vol. 67, pp. 200–205, 2012.

[32] C. S. Fischer and J. Luecker, "Propagators and phase structure of Nf=2 and Nf=2+1 QCD," 2012.

[33] J. A. Mueller, C. S. Fischer, and D. Nickel, "Quark spectral properties above Tc from Dyson-Schwinger equations," *Eur.Phys.J.*, vol. C70, pp. 1037–1049, 2010.

[34] C. DeTar and U. Heller, "QCD Thermodynamics from the Lattice," *Eur.Phys.J.*, vol. A41, pp. 405–437, 2009.

[35] J. I. Kapusta and C. Gale, *Finite-temperature field theory : principles and applications.* Cambridge University Press, 2 ed., Aug. 2006.

[36] S. Borsanyi *et al.*, "Is there still any T_c mystery in lattice QCD? Results with physical masses in the continuum limit III," *JHEP*, vol. 1009, p. 073, 2010.

[37] M. Le Bellac, *Thermal field theory.* Cambridge monographs on mathematical physics, Cambridge: Cambridge Univ. Press, 1996.

[38] W. H. Press, S. A. Teukolsky, W. T. Vetterling, and B. P. Flannery, *Numerical recipes in C (2nd ed.): the art of scientific computing.* New York, NY, USA: Cambridge University Press, 1992.

[39] C. S. Fischer, A. Maas, and J. A. Muller, "Chiral and deconfinement transition from correlation functions: SU(2) vs. SU(3)," *Eur.Phys.J.*, vol. C68, pp. 165–181, 2010.

List of Figures

Erklärung

Hiermit erkläre ich an Eides statt, dass ich die vorliegende Master-Thesis selbstständig verfasst und keine anderen als die angegebenen Quellen und Hilfsmittel benutzt habe.

Gießen, den October 16, 2012

Christian Welzbacher